Mechanisms of extension at nonvolcanic margins: Evidence from the Galicia interior basin, west of Iberia

M. Pérez-Gussinyé,[1] C. R. Ranero, and T. J. Reston
GEOMAR Research Center for Marine Geosciences, Kiel, Germany

D. Sawyer
Department of Geology and Geophysics, Rice University, Houston, Texas, USA

Received 18 July 2001; revised 28 March 2002; accepted 9 May 2002; published 14 May 2003.

[1] We have studied a nonvolcanic margin, the West Iberia margin, to understand how the mechanisms of thinning evolve with increasing extension. We present a coincident prestack depth-migrated seismic section and a wide-angle profile across a Mesozoic abandoned rift, the Galicia Interior Basin (GIB). The data show that the basin is asymmetric, with major faults dipping to the east. The velocity structure at both basin flanks is different, suggesting that the basin formed along a Paleozoic terrain boundary. The ratios of upper to lower crustal thickness and tectonic structure are used to infer the mechanisms of extension. At the rift flanks (stretching factor, $\beta \leq 2$) the ratio is fairly constant, indicating that stretching of upper and lower crust was uniform. Toward the center of the basin ($\beta \sim 3.5-5.5$), fault-block size decreases as the crust thins and faults reach progressively deeper crustal levels, indicating a switch from ductile to brittle behavior of the lower crust. At $\beta \geq 3.5$, faults exhume lower crustal rocks to shallow levels, creating an excess of lower crust within their footwalls. We infer that initially, extension occurred by large-scale uniform pure shear but as extension increased, it switched to simple shear along deep penetrating faults as most of the crust was brittle. The predominant brittle deformation might have driven small-scale flow ($\leq$40 km) of the deepest crust to accommodate fault offsets, resulting in a smooth Moho topography. The GIB might provide a type example of nonvolcanic rifting of cold and thin crust. *INDEX TERMS:* 8109 Tectonophysics: Continental tectonics—extensional (0905); 8105 Tectonophysics: Continental margins and sedimentary basins; 3025 Marine Geology and Geophysics: Marine seismics (0935); 8159 Tectonophysics: Rheology—crust and lithosphere; 8020 Structural Geology: Mechanics; *KEYWORDS:* nonvolcanic rifting, marine seismics, lower crust rheology

Citation: Pérez-Gussinyé, M., C. R. Ranero, T. J. Reston, and D. Sawyer, Mechanisms of extension at nonvolcanic margins: Evidence from the Galicia interior basin, west of Iberia, *J. Geophys. Res.*, *108*(B5), 2245, doi:10.1029/2001JB000901, 2003.

1. Introduction

[2] The way extensional strain is distributed in space and time within the lithosphere is not yet fully understood. In map view, the width of the rifting region is thought to be controlled by the thermal structure of the lithosphere at the initiation of rifting. Wide rifts ($\sim$500–700 km, e.g., the Basin and Range) may form where the crust was originally warm and thick ($\geq$40 km); narrow ones ($\leq$100–200 km, e.g., the Gulf of Suez) may form where the crust was originally cold and thin ($\sim$30 km) [*Buck*, 1991; *Bassi*, 1995; *Hopper and Buck*, 1996]. The extension rate may also influence the extent of the rifting region [*England*, 1983; *Sonder and England*, 1989] if the initial thermal structure of the lithosphere is warm [*Bassi*, 1995].

[3] In cross section an apparent discrepancy exists between the amount of stretching measured from upper crustal faulting and that determined from measured crustal thickness and/or subsidence. This has led to the suggestion that the distribution of extension may vary between the upper and lower crust (UC and LC). Where the initial crust was warm and thick ($\geq$40 km), such as the Basin and Range, extension of the upper crust with no associated Moho topography has been explained by large-scale (>100 km) lower crustal flow toward the extending regions [*Gans*, 1987; *Block and Royden*, 1990; *Kruse et al.*, 1991]. This flow may be driven by pressure gradients induced by the topographic differences between the extending and the unextended region [*Artyushkov*, 1973].

[4] Where the crust was cold and thin prior to rifting ($\sim$30 km thick crust), the amount of extension inferred elsewhere from measurements of brittle faulting is generally less than that measured from overall crustal extension (as obtained from wide-angle seismic data and/or subsidence data). This has led to the hypothesis that the upper crust and

[1] Now at Department of Earth Sciences, Oxford University, Oxford, UK.

0148-0227/03/2001JB000901$09.00

lower crust become decoupled to let the lower crust and mantle stretch more than the upper crust at the center of the rift. This decoupling has been explained in two ways: (1) by displacement of upper and lower crust along a detachment at the brittle-ductile transition which migrates upward during rifting and shoals close to the surface at the region of maximum thinning (e.g., Northern Carnarvon Basin, Australia, West Iberia margin) [*Driscoll and Karner*, 1998]. This implies that most crust remains ductile during the entire rifting, and (2) by nonuniform pure shear extension in which the ductile, weak lower crust is squeezed out of the center of the basin at the beginning or during the entire rifting period (West Iberia margin; see *Whitmarsh et al.* [2001] and *Brun and Beslier* [1996], respectively). These models predict a large deficit of lower crust at the center of the extending region and large-scale differential stretching of upper and lower crust along a horizontal scale of at least hundred kilometers.

[5] An alternative model for deformation at cold nonvolcanic margins suggests that neither decoupling nor large-scale differential stretching of upper and lower crust occur during the entire rifting period. In this model, as in that proposed by *Whitmarsh et al.* [2001], the upper and lower crust become tightly coupled at the late stages of rifting as the lower crust enters the brittle deformation regime [*Pérez-Gussinyé and Reston*, 2001]. However, *Pérez-Gussinyé and Reston* [2001] suggest that the embrittlement of the lower crust occurs progressively during the entire rifting period as the upper and lower crust thin by similar amounts. This change in the rheological properties of the lower crust is accompanied by a change from large-scale pure shear extension to large-scale nonuniform pure shear along a decollement formed between crust and mantle at the last stages of extension (e.g., Porcupine Basin [*Reston et al.*, 2001], West Iberia margin [*Reston et al.*, 1996; *Krawczyk et al.*, 1996; *Pérez-Gussinyé and Reston*, 2001]). Throughout this paper "large-scale" refers to processes which occur at a horizontal scale of $\geq$100 km, and "small-scale" refers to lateral distances of $\leq$50 km. "Uniform pure shear" indicates thinning of the upper crust, lower crust, and mantle by similar amounts. "Nonuniform pure shear" indicates differential stretching either between upper and lower crust or between crust and mantle.

[6] The nonvolcanic margin off West Iberia is one of the best studied examples of rifting that initiated within cold and thin crust as it has been the subject of three Ocean Drilling Program (ODP) drillings and numerous geophysical surveys [*Whitmarsh and Wallace*, 2001; *Dean et al.*, 2000; *Reston et al.*, 1996, and references therein]. However, most of these surveys have been concentrated at the areas of maximum crustal thinning ($\beta > 4-6$) and at the continent-ocean transition (COT) and were aimed to understand the nature of the COT and the mechanisms by which breakup of thin continental crust ($\sim$7 km) leads to exposure of mantle at the COT. Less extended areas are little studied, and there is a lack of crustal-scale cross sections extending from the continental shelf to the edge of the continental crust. To shed light on the controversy on the mechanisms of crustal thinning, we studied a multichannel seismic (MCS) prestack depth-migrated section and a coincident wide-angle seismic velocity model across the entire the Galicia Interior Basin (GIB, Figure 1). The seismic reflection images and wide-angle seismic information provide the tectonic and velocity structure of the basin and show the deformation of the upper and lower crust from the slightly extended rift flanks (stretching factors, $\beta \sim 1.5$), to the center of the basin, ($\beta \sim 3.5-5.5$). Additionally, we used numerical modeling results on the rheological evolution of the crust and on the thermal limits for large-scale lower crustal flow to constrain the mode of deformation during extension. The Galicia Interior Basin may provide a type example for rifting within relatively cold and thin crust. Thus the mechanisms of extension that formed the basin might explain the structure of other nonvolcanic margins of the North Atlantic.

[7] The GIB is located between the continental shelf and Galicia Bank extending approximately N-S along more than 100 km offshore West Iberia (Figure 1). The basin is thought to be the northward continuation of the onshore Lusitanian Basin [*Wilson et al.*, 1990], which is bounded to the east by the Porto-Tomar fault, which separates different terrains of the Variscan orogeny [*Capdevila and Mougenot*, 1988]. *Murillas et al.* [1990] indicate that extension at the GIB occurred from Tithonian to Valanginian time (152–132 m.y. following the timescale of *Gradstein et al.* [1994]). During Tithonian to Hauterivian times (152–137 m.y.), reef carbonates were deposited across the basin, indicating that the crust had been only slightly thinned. The main rifting phase took place during Valanginian time [*Murillas et al.*, 1990]. Subsequently, extension stopped in the GIB and shifted to Galicia Bank and to the Deep Galicia Margin where final continental breakup occurred in late Aptian ($\sim$112 m.y. [*Boillot and Winterer*, 1988]).

2. Data Acquisition

[8] During the Iberia Seismic Experiment aboard the R/V *Maurice Ewing* (July to August 1997) coincident wide-angle and MCS data were simultaneously acquired along profile 17 (Figure 1). To acquire MCS data, a 160-channel 4-km streamer was used along most of the line (line 17W in Figure 1). However, near the coast (east of 10°W) a 40-channel, 1-km streamer was used because of the heavy ship traffic (line 17E in Figure 1). The wide-angle data were recorded on seven ocean bottom hydrophones (OBH) from GEOMAR [*Flueh and Bialas*, 1996], evenly spaced at a distance of 22.5 km. OBH 241 located at the eastward slope of Galicia Bank did not record data. A tuned 20 air gun array source was used with a total capacity of 130 L. Shots were fired at a compromise time interval for the acquisition of MCS and wide-angle data of $\sim$40 s, corresponding to a shot spacing of 100 m. This geometry yielded a 20-fold stack for MCS line 17W, and a fivefold stack for MCS line 17E.

3. Multichannel Seismic Reflection Data

3.1. Analysis of the Data

[9] The main steps in the processing sequence of line 17W were statistical deconvolution, velocity analysis, multiple removal, a second velocity analysis, and time migration. The statistical deconvolution was computed using a single-trace, Wiener operator. Within each trace, two 2-s-long overlapping windows were designed for the computa-

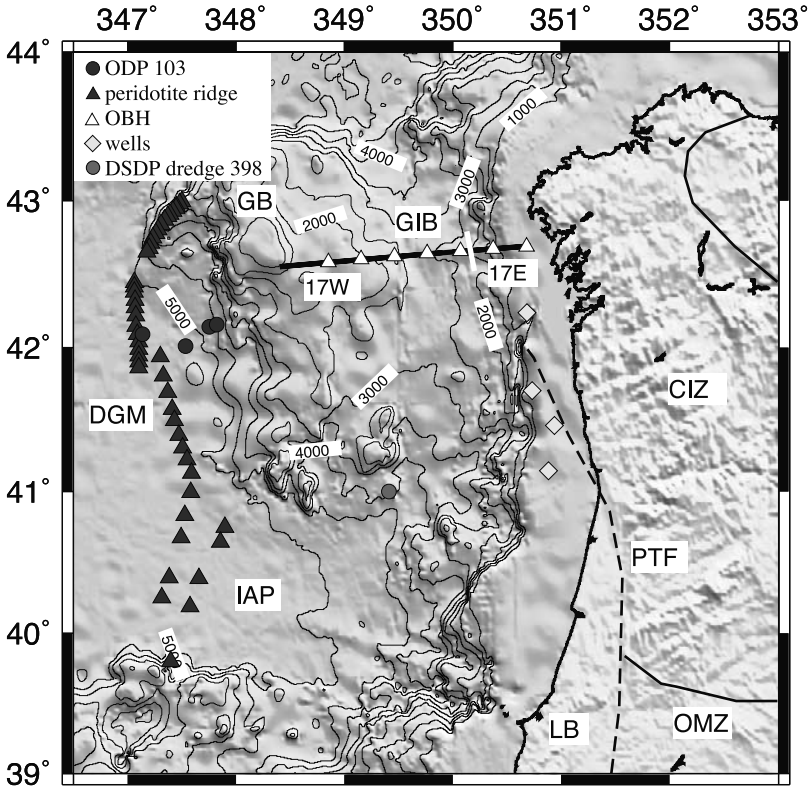

Figure 1. Bathymetry and topography map of West Iberia [*Smith and Sandwell*, 1995]. Continental breakup occurred along the Iberia Abyssal Plain (IAP) and the Deep Galicia Margin (DGM). Galicia Bank (GB) separates the Galicia Interior Basin (GIB) from the Deep Galicia Margin. ODP drilling 103 (dark gray circles), several wells (diamonds), and dredges (DSDP Leg 398, light gray circle) helped constrain the seismic stratigraphy at the GIB [*Murillas et al.*, 1990]. White triangles are ocean bottom hydrophones deployed along line 17. Line 17E was shot with a 1-km-long streamer, and line 17W was shot with a 4-km-long streamer. The onshore Variscan terrains are shown: LB, Lusitanian Basin; OMZ, Ossa Morena zone; CIZ, Central Iberian zone. The Porto-Tomar fault (PTF) is a shear zone separating these terrains. Its northward continuation is believed to run offshore along the GIB [*Capdevila and Mougenot*, 1988].

tion of the deconvolution operator. The first window was in the sediments, and the second was in the basement to allow for the change in frequency with increasing travel time. Each operator was applied at 100% in the center of each window and interpolated in between. Velocity analyses were performed twice, once after statistical deconvolution and a second after multiple removal.

[10] Multiples in deep water are difficult to attenuate: usually, the amplitudes of primary reflections at the multiple's two-way travel time are weak. Additionally, the shooting interval of 100 m led to a distance between traces of 200 m within a common midpoint (CMP), which caused serious problems of spatial aliasing. To attenuate the multiple, two frequency-wave number (FK) filters and a weighted stack in the CMP gathers were applied. The first FK filter was applied to the CMP gathers after normal moveout (NMO) correction with water velocity in order to flatten the seafloor multiple, so that it plots at zero dip in the FK domain avoiding spatial aliasing. A narrow FK filter was designed to filter out the 0° dip arrivals. The second FK filter was designed using the same strategy but using a NMO velocity of 1700 m/s to filter out the multiple of sediments. A weighted stack was applied to every CMP gather after NMO correction with stacking velocities. At every time sample this process compares the amplitude of every trace within a CMP gather with the amplitude of the stacked trace of the corresponding CMP gather. The samples with amplitude very different from the stacked trace are weighted down. Hence amplitudes that are not laterally consistent along the gather; in particular, the remains of the multiple, are attenuated. An inner trace mute was applied to remove the multiples at near offsets. After stacking, multiples of strongly dipping layers were still present, and surgical FK filters were applied to the stacked section to further attenuate them.

[11] The time migration was accomplished in two steps. First, the data were migrated with constant water velocity using a finite difference algorithm in the frequency space domain. After water velocity migration, side swipes and remaining multiples collapsed, and their amplitudes were surgically weighted down. Second, a cascaded migration was applied using a finite difference algorithm on the time-space domain. This migration was performed with a smoothed and geologically reasonable version of the stacking velocity model.

[12] Along line 17E the fivefold CMP gathers prevented FK multiple removal before stacking because the NMO was too small to discriminate primaries from multiples. The rest

of the processing sequence is similar to that used for line 17W. The final time migrations of line 17W and 17E are shown in Figure 2 (enlarged version of Figure 2 is available as auxiliary material[1]). A high-quality poststack time migration is fundamental to help interpret the data during the iterations of prestack depth migration.

[13] At rifted margins, faulting produces a complex basement topography and, within the tilted blocks, strongly dipping layers that are difficult to image by conventional processing techniques because of rapid lateral and vertical changes in velocity. To obtain a geometrically correct image, in-depth the data were prestack depth migrated. This method not only produces a section in depth but also corrects for ray path bending at velocity interfaces and gradients following Snell's law [*Hubral*, 1977] and avoids CMP smearing.

[14] For prestack depth migration a geological velocity model is necessary. The model was iteratively constructed by depth-focusing error analysis of reflected and diffracted energy at closely spaced intervals (80 m) along the profile and common reflection gathers [*Sherwood*, 1989; *Denelle et al.*, 1986]. The velocity model was built up from top to bottom one layer at a time since the velocity of the overburden affect those determined for deeper levels. Focusing analysis only gives reliable velocity information where there are continuous reflections and also where the reflectors are not too deep so that offset-dependent velocity information is obtained. Beneath top basement, clear reflections are only locally observed, and Moho reflections are too deep for velocity estimation. Therefore beneath top basement, velocity information obtained with focusing analysis was complemented with wide-angle velocities to create the macrovelocity model for the prestack depth-migrated section in Figure 2.

3.2. Description of the MCS Data

3.2.1. Sedimentary Infill

[15] The sedimentary deposits reach a thickness of ~6 km at the center of the basin (km ~115 and ~130, Figure 2) and thin toward Galicia Bank and the continental slope, thickening locally at small basins formed over rotated blocks. The sediment infill is separated by a regional unconformity with strongly reflective, horizontally layered sequences above and more transparent sedimentary sequences below (boundary between formations 3 and 4, Figures 2 and 3). The upper sequences onlap the previous topography, indicating that they were deposited after the tectonic activity that formed the topography. Correlation of the upper sequences with those interpreted by *Murillas et al.* [1990] on a line oblique to line 17 indicates that they consist of three sedimentary formations (formations 1–3) deposited during Cenomanian to present [*Pérez-Gussinyé*, 2000]. *Murillas et al.* [1990] interpreted the regional unconformity separating upper and lower sequences as equivalent to the latest Aptian unconformity formed during breakup at the Deep Galicia Margin, west of Galicia Bank. Below the latest Aptian unconformity, two sedimentary formations are recognized. At the center of the basin (km 70 to 150, Figures 2 and 3), formation 4 (Hauterivian to late Aptian, 132–112 m.y. [*Murillas et al.*, 1990]) appears horizontally layered and onlaps the previous topography, indicating that it is postrift to the extension at the GIB. However, on the east flank of Galicia Bank (km 0–70, Figure 2), formation 4 occurs on top of eastward tilted blocks and was deposited during movement of westward dipping faults [*Murillas et al.*, 1990] (Figure 2). This extensional phase, which affected the east flank of Galicia Bank but not the center of the GIB, is coeval with that leading to breakup at the Deep Galicia Margin.

[16] The main extensional phase within the GIB occurred during deposition of formation 5 (Valanginian, 137–132 m.y. [*Murillas et al.*, 1990]). This unit fills the lows formed by large tilted blocks bounded by eastward dipping faults and locally forms wedge like fans (e.g., CMP 6700 to 7200, Figure 2), indicating that it was deposited during movement of those faults (km 70–150, Figures 2 and 3). Shallow water carbonates (Tithonian to Berrasian, 152–137 m.y.) drilled across the margin [*Murillas et al.*, 1990, and references therein] are a few hundred meters thick and have high velocities and may be incorporated in our interpretation of top basement.

3.2.2. Basement

[17] The crystalline basement has an asymmetric tectonic structure (Figure 2). Whereas top basement to the east of the basin (zone I, Figure 2) gradually deepens toward the center of the basin, the deepest part of the basin (zone II, Figure 2) is characterized by large basement offsets with blocks (B1–B5, Figures 2 and 3) rotated along eastward dipping faults active during the Valanginian extensional episode (F1–F6, Figures 2 and 3). Block size decreases toward the center of the basin accompanied by a decrease in fault spacing. Faults are planar and dip at an angle of ~35° with offsets of top basement of up to 2 km (faults F5 and F3, Figures 2 and 3). Planar faults have also been observed on deep seismic data over other rift basins (see review by *Kusznir et al.* [1995]) and are supported by earthquake seismology [*Jackson*, 1987; *Braunmiller and Nábèlek*, 1996]. Toward the east flank of Galicia Bank (zone III, Figure 2), top basement shallows and a second generation of west dipping Hauterivian to Aptian faults is observed. A zone of complex structure occurs between km 35 and km 55, where both extensional phases were active (Figure 2).

[18] Within the basement of zone II a set of strong, gently dipping reflections appears at km 70 to 100 (DR reflections in Figures 2 and 3). This reflectivity is not observed at zones I and III where extension factors are smaller (Figure 4b shows the stretching factors along line 17). The occurrence of a similar reflectivity pattern as extension factors increase toward the axis of the basin is also observed on reprocessed industry data in the same area [*Pérez-Gussinyé*, 2000].

[19] Within zones III and I, a set of strong, subhorizontal, low frequency reflections occur at wide-angle Moho depths (Figure 2). Toward the center of the basin (km 70 to 100, Figure 2), there are no obvious Moho reflections; however, a set of strong reflections, dipping away from the center of the basin, occurs at km ~80 to ~100 at 16–20 km depth

[1]Enlarged version of Figure 2 is available via Web browser or via Anonymous FTP from ftp://agu.org/apend/jb/2001JB000901 (Username = "anonymous", Password = "guest"); subdirectories in the ftp site are arranged by paper number. Information on searching and submitting electronic supplements is found at http://www.agu.org/pubs/esupp_about.html. http://www.agu.org/pubs/esupp_about.html

(Figure 2), which coincides with the Moho defined from wide-angle data.

4. Wide-Angle Data

4.1. Analysis of the Data

[20] Processing of the wide-angle data consisted of deconvolution and offset- and time-dependent band-pass filtering. Deconvolution was aimed at increasing the resolution to image the near-offset reflections from sedimentary layers and top basement. A single-trace, statistical Wiener deconvolution was applied with a prediction length of 80 ms and a zero phase characteristic in order to avoid time shifting of the signal. The length of the operator was chosen to be long enough to avoid changing the source wavelet shape but to attenuate the reverberations that obscure the primary reflections from sediment layers and top basement in the near offsets. The filter was computed using a 480-ms-long operator designed over a 2-s-long window, so that different operators were computed along the trace. The operators were applied at 100% at the center of each window and interpolated in between. The frequency filter was designed to retain relatively high frequencies (3/5 to 35/50 Hz) for near offsets and short travel times and to progressively filter out high frequencies as the offset and travel time increased. The narrowest band-pass filter applied was 3/5 to 10/20 Hz.

[21] Picking the onset of far-offset arrivals was accomplished using both the processed and the raw data. For the near offsets we used the processed data alone. Uncertainty in travel time picking is 50 ms for arrivals from the sedimentary and upper basement layers (*Ps* and *Pg* in Figures 5–11). The uncertainty in picking arrivals from the mid and lower crust is 100 ms (*Pmc* and *Plc* in Figures 5–11) and 120 ms for the mantle (*PmP* and *Pn* in Figures 5–11).

4.2. Modeling Procedure

[22] Wide-angle data were interactively forward modeled using the program MacRay [*Luetgert*, 1992]. Additionally, the MCS data were used to constrain the depth of the sedimentary units and top basement between OBH positions [*Kopp*, 1997]. Figure 12 shows the OBH near-offset reflections and the horizons of the MCS time section that were used to constrain the wide-angle data. These horizons correspond approximately to the boundaries between the five sedimentary formations in Figure 2.

[23] The wide-angle model was constructed one layer at a time. The depth and velocities of the shallow sedimentary layers and top basement were found by matching the near-offset reflections and refractions in the wide-angle data. The MCS horizons were used to constrain the depth to the these layers between OBH positions. Below top basement only wide-angle data were used with exception of the MCS Moho reflection. This was used to extrapolate the wide-angle model where there was no information from the wide-angle data, between km ~30–45 and ~175–185 (Figure 12). Later, the wide-angle model was cross checked against and partly rebuilt using the prestack depth-migrated section where the imaging of top basement was better than in the time-migrated section (compare top basement at block B5 in the depth and time-migrated sections, Figure 2).

4.3. Velocity Structure From Wide-Angle Data

[24] The resulting velocity model has a sedimentary cover up to 6 km thick (zone II, Figure 4) with five sedimentary units similar to those in the MCS profile (Figure 2). The crystalline crust beneath the continental shelf (zone I) and under the east flank of Galicia Bank (zone III) thins from ~24 km and ~21 km, respectively, to around ~6–8 km at the center of the basin (zone II) and displays an asymmetric structure (Figure 4). The velocity structure has been modeled with three velocity layers in zone I and two velocity layers in zones II and III (Figure 4a). At zone I the upper, middle, and lower layers have velocities that range from ~5 to 6 km/s, 6.1 to 6.2 km/s, and ~6.6 to 6.9 km/s, respectively. At zones II and III the upper and lower layers have velocities ranging from ~5.2 to 6.3 km/s and ~6.6 to 6.9 km/s, respectively.

4.3.1. Sedimentary Layers

4.3.1.1. Zone I

[25] Reflections from the sedimentary layers were not observed either on OBH 236 or on OBH 237 (Figures 5 and 7). In this area the velocity of the sedimentary layers was found by matching the wide-angle *Ps* refractions, and so their thicknesses are not well constrained. The depth of top basement was constrained by the MCS data. Sediment thickness is ~0.3 km at the continental shelf and locally increases to 0.8–2.3 km in small basins (km 154–170 and 174–183 in Figure 4).

4.3.1.2. Zone II

[26] Reflections from five sedimentary units were identified on OBHs 238, 239, and 240 (Figures 8, 9, and 10). The three youngest units coincide with postrift formations 1 + 2, 3a, and 3b of *Murillas et al.* [1990] (see Figure 12). Their velocities increase gradually without strong velocity contrasts (1.8 to 2.9 km/s, 3.1 to 3.3 km/s, and 3.35 to 3.4 km/s). The base of the third unit coincides with the latest Aptian unconformity in the MCS data (Figures 2, 3, and 12) and corresponds to a large velocity jump.

[27] The correspondence between units 4 and 5 and formations 4 and 5 is approximate; unit 4 corresponds to formation 4, underneath OBH 239 (Figures 9 and 12), but beneath OBH 238 (Figures 8 and 12) the bottom of unit 4 is shallower than for formation 4. Unit 4 has velocities ranging from 3.8 to 4.3 km/s. Unit 5 corresponds to sedimentary formation 5 at OBH 239 and has a velocity from ~4.7 to ~4.9 km/s. The match between time-stratigraphic formations and the velocity-defined units is remarkably good and may imply that the unconformities separate formations with different degrees of lithifaction.

4.3.1.3. Zone III

[28] In this area the sedimentary cover thins to ~1 km, although it thickens locally up to 2.8 km in half grabens formed above over tilted blocks (Figure 4). On OBH 242 (Figure 11) only four wide-angle reflected phases were identified, which approximately correspond to formations 1 + 2, 3a, 3b, and 4 in the MCS data (Figure 12).

4.3.2. Basement-Crystalline Crust

4.3.2.1. Zone I

[29] In this area the basement consists of three velocity layers under the continental shelf and slope (Figure 4). OBH

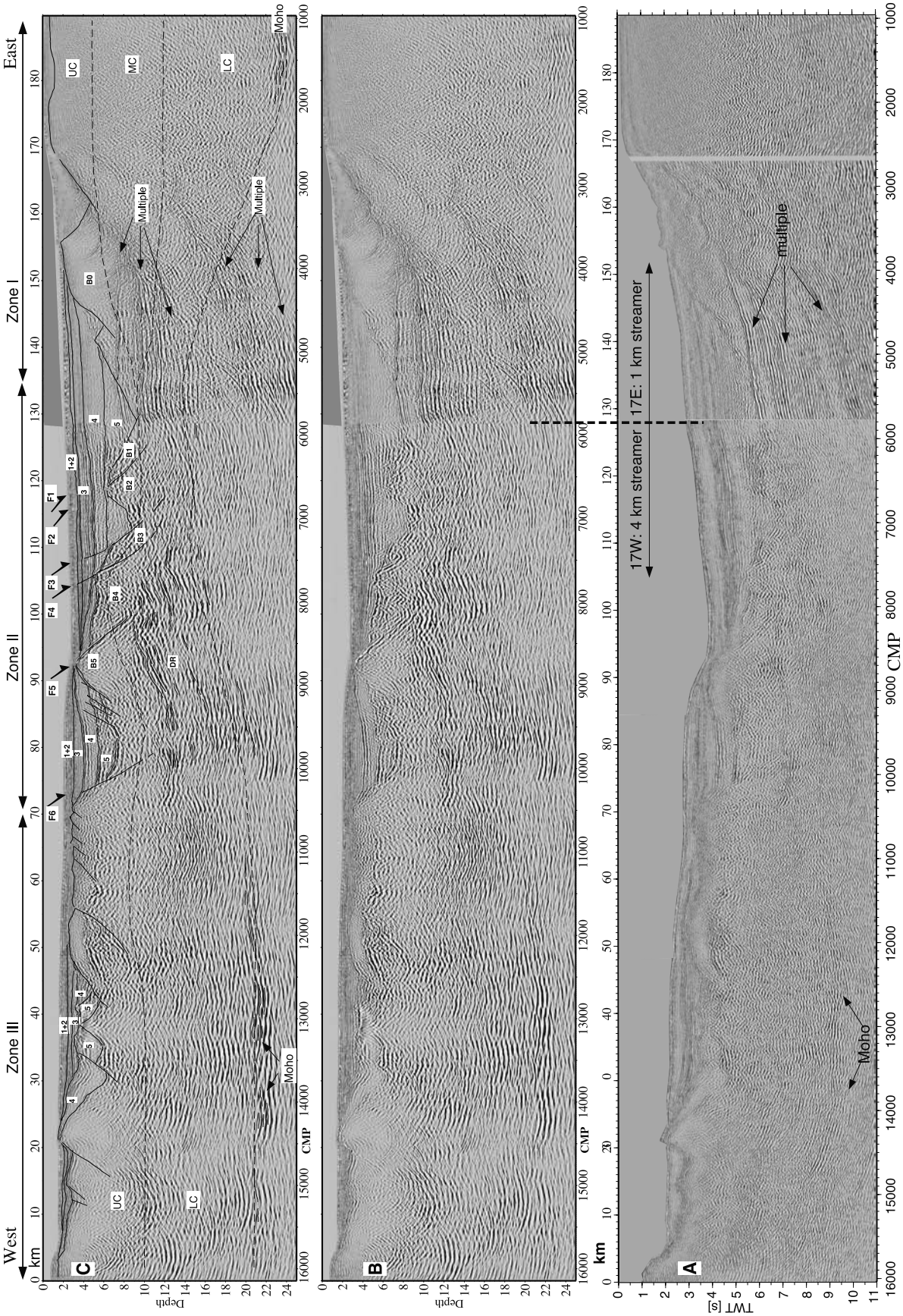
West
Zone III
Zone II
Zone I
East
km
CMP
Depth
TWT [s]
A
B
C
UC
LC
MC
Moho
Multiple
multiple
17W: 4 km streamer
17E: 1 km streamer
Bo
B1
B2
B3
B4
B5
DR
F1
F2
F3
F4
F5
F6

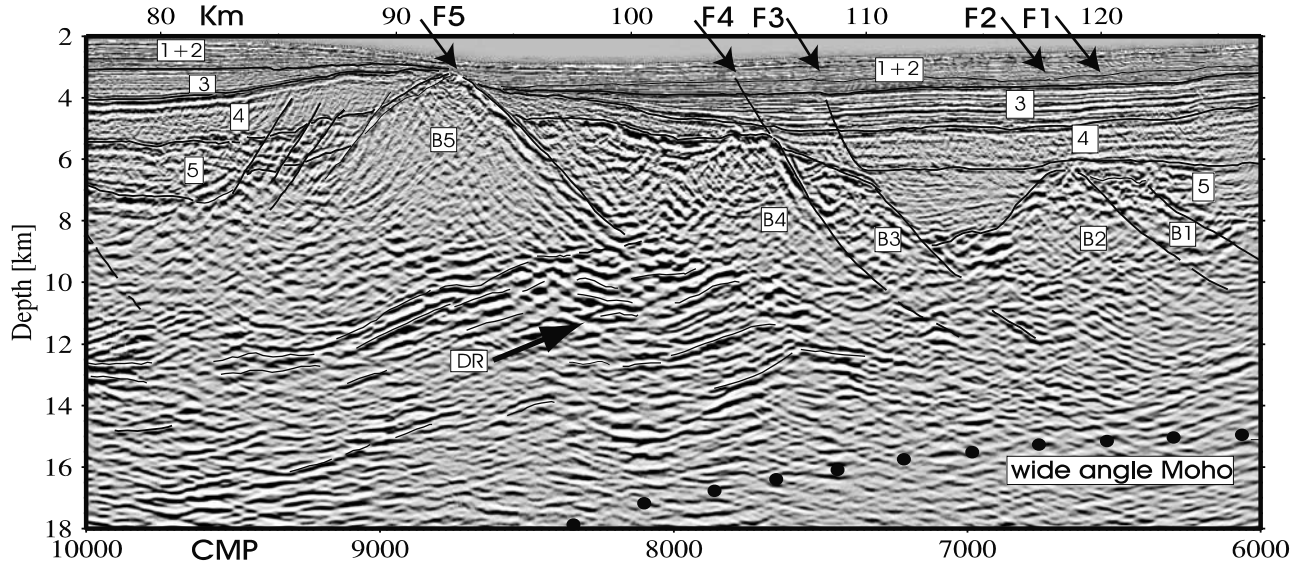

Figure 3. Blowup of the prestack depth migration between CMPs 6000 and 10000, overlain by a geological interpretation (solid lines) and Moho defined by wide-angle data (black dots). Numbers indicate sedimentary formations. F1–F5 are faults that bound rotated blocks B1–B5. DR are deep reflections in the lower crust.

237 shows three different slopes of refracted waves traveling through each of these layers (*Pg*, *Pmc*, and *Plc* in Figure 7) with velocities ranging from 5 to 6 km/s, 6.1 to 6.2 km/s, and 6.6 to 6.9 km/s, respectively. On OBH 236 a weak reflection from the top of the third layer is observed (*PlcP* in Figure 6). Toward the center of the basin the layers thin and their velocity gradient increases.

[30] The basement refracted arrivals observed on OBHs 236 and 237 could also be modeled assuming a two-layer structure with the upper crustal layer with velocities from 5 to 6 km/s and a lower crustal layer with lateral constant velocities of 6.2 to 6.9 km/s. However, these lower crustal velocities are too low to match the lower crustal arrivals observed on OBHs 238 and 239, which indicate velocities of ~6.6 to 6.9 km/s (see below). Also, rays traveling through a model with two velocity layers with a lower crust velocity of 6.2 to 6.9 km/s at zone I and 6.7 to 6.9 at zone II match worse the observed refracted arrivals through the basement at OBH 236 and 237 than the three-layer model. We used the two-dimensional ray tracing of *Zelt and Smith* [1992] to calculate the root-mean-square residual misfit (T_{RMS}) for the refracted rays in the lower crust for OBHs 236, 237, 238, and 239. The T_{RMS} obtained assuming a three-layer model is 0.144 s, and for the latter two-layer model is 0.169 s. Therefore, adding an intermediate layer beneath the continental shelf and slope with a low gradient and velocities of 6.1–6.2 km/s as shown here attains the best fit model. This velocity structure also fits the weak *PlcP* reflection observed on OBH 236 (Figure 6). The depth to the Moho is controlled in this area by the *PmP* reflection observed on OBH 236 (Figure 5) and by matching the reflections from the Moho in the MCS profile (Figures 2 and 12). The crust is 24 km thick beneath the shelf and thins progressively toward the center of the basin.

4.3.2.2. Zone II

[31] In contrast to zone I, west of km 130, high velocities of ~6.6 km/s are found at shallow depths within the basement, and only two velocity gradients are observed. This velocity structure is modeled with two layers required to match the refraction arrivals at OBHs 238, 239, and 240 (*Pg* and *Plc* arrivals in Figures 8, 9, and 10). At the deepest part of the basin the crystalline crust has a minimum thickness of ~6 km (km 130, Figure 4). The velocity of the upper layer increases from 5.3 km/s at the top to 6.3 km/s at the bottom, with a high velocity gradient (0.3 s^{-1}). This layer thins notably at km 113 and 130, coinciding with basement lows. The lower crustal layer reaches a minimum thickness of ~5 km at the center of the basin (km 111 to 130, Figure 4) and has a velocity of 6.6 km/s at the top and 6.9 km/s at the bottom (Figures 8, 9, and 10). Both upper and lower layers thicken, and their velocity

Figure 2. (opposite) (a) Poststack time migration of line 17. On line 17E it was not possible to attenuate the multiple because the short streamer and the shooting interval yielded a fivefold stack. (b) Prestack depth migration of line 17W and poststack depth migration of line 17E. (c) Depth migration of line 17 overlain by a geological interpretation (solid lines) and velocity layers defined by the wide-angle data (stippled lines): UC (upper crust), MC (middle crust), LC (lower crust). Zones I, II, and III differ in their structural style and their velocity structure (see Figure 4). Numbers indicate sedimentary formations. F1–F6 are faults that bound rotated blocks B1–B5. DR are deep reflections in the lower crust. B0 is the basement at the continental slope area. (The enlarged Figure 2 is available as auxiliary material.)

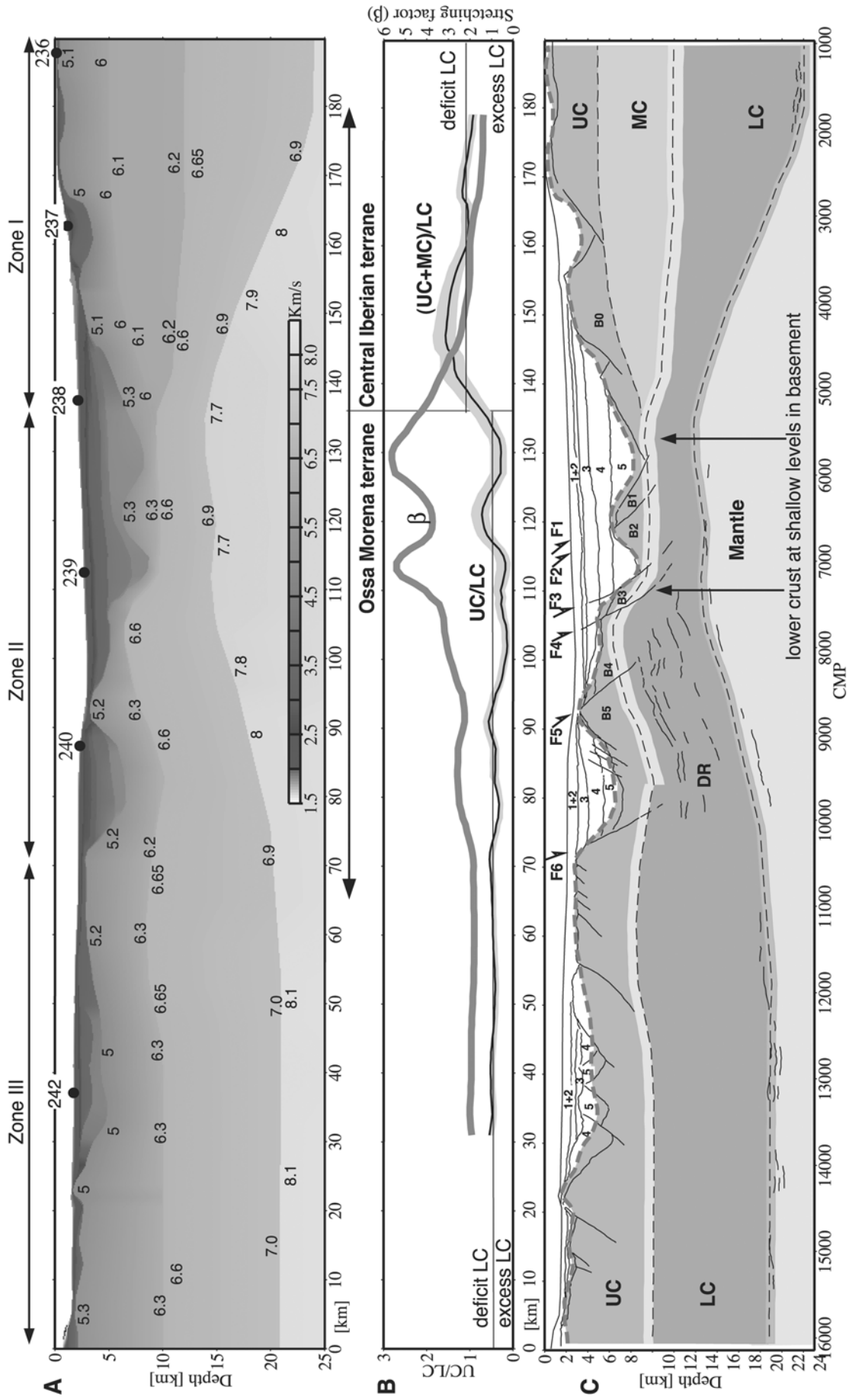
Zone I
Zone II
Zone III
Ossa Morena terrane
Central Iberian terrane
Km/s
A
Depth [km]
[km]
B
UC/LC
deficit LC
excess LC
(UC+MC)/LC
UC/LC
Stretching factor (β)
C
UC
MC
LC
DR
Mantle
lower crust at shallow levels in basement
CMP

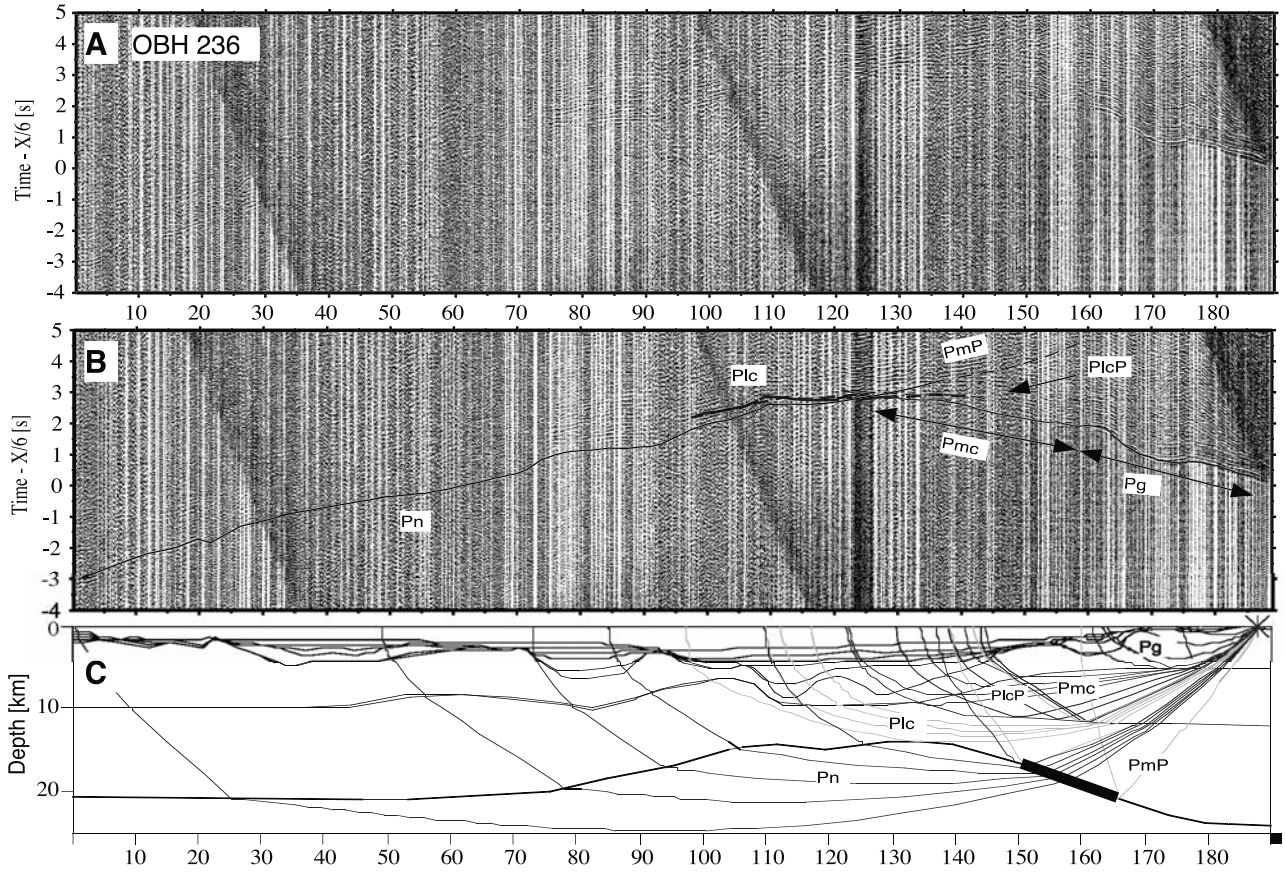

Figure 5. (a) Processed record section of OBH 236. (b) Processed record section overlaid by calculated travel time arrivals. (c) Ray tracing for identified phases: *Pg*, *Pmc*, *Plc*, and *Pn* are refracted arrivals through the upper, middle, and lower crust and through the mantle, respectively. *PlcP* and *PmP* are reflections from top lower crust and Moho. Thick black line at Moho is the segment controlled by the data in the figure.

gradient decreases toward the west. The depth of the Moho in zone II is constrained by *PmP* arrivals observed by OBHs 237, 239, and 240 (Figures 7, 9, and 10).

4.3.2.3. Zone III

[32] The eastern flank of Galicia Bank has also a two-layer velocity structure. Refracted and reflected arrivals observed at OBHs 240 and 242 (Figures 10 and 11) indicate that the velocity in the upper crustal layer ranges from 5–5.3 km/s at the top to 6.3 km/s at the bottom and has an average thickness of 5 km. The lower crustal layer has an average thickness of 10 km and is characterized by velocities increasing downward from 6.65 to 6.9 km/s just above the Moho. The depth to the Moho (21 km in this area) is constrained by *PmP* arrivals observed at OBH 240 (Figure 10) and reflections in the near vertical data.

4.4. Uncertainty of the Velocity Model

[33] The top of the lower crustal layer in zones II and III is not well constrained since no reflections are observed from this interface. To obtain the range of possible depths that would still fit the data, assuming a 100 ms of picking

Figure 4. (opposite) (a) Two-dimensional velocity structure from forward modeling of wide-angle data. Numbers are velocities in km/s. The basement consists of three velocity layers at the continental shelf and slope and of two layers at the center and west flank of the basin. Zones I, II, and III differ in their structural style and their velocity structure (see also Figure 2). (b) Dark gray line is stretching factor (β) defined as the ratio of crystalline crust (thickness from top basement to Moho from wide-angle data) to the crust onshore. UC, MC, and LC are upper, middle, and lower crust defined from wide-angle data. Black line is ratio of UC to LC (at the Ossa Morena terrain) and of UC + MC to LC (at the Central Iberian terrain, see discussion). The underlying gray shading indicates the variation of this ratio taking into account the depth uncertainties in the location of the top LC and Moho (see Figure 13). Both the stretching factor and upper to lower crustal ratio are shown where the ray coverage is good. (c) Geological interpretation (black lines) and wide-angle layers (dashed lines). The gray shading at the top of lower crust and Moho indicates calculated depth uncertainties of these interfaces. F1–F6 are faults bounding rotated blocks B1–B6. Numbers are sedimentary formations.

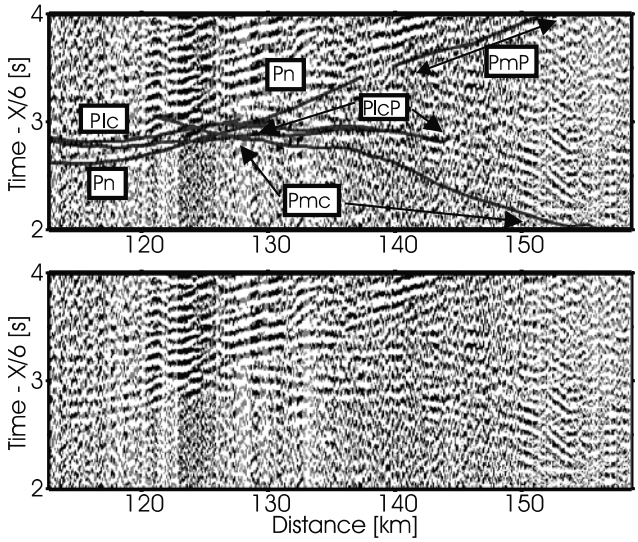

Figure 6. Blowup of processed record section of OBH 236. See weak *PlcP* reflection between km 130 and 140.

uncertainty, we calculated the root-mean-square residual misfit (T_{RMS}) for a set of models (Figure 13). For this we used the two-dimensional ray tracing of *Zelt and Smith* [1992] for forward modeling. Each model consisted of varying the depth of the top of the lower crustal layer at a particular area while maintaining the velocity gradient above and below. Then the T_{RMS} misfit for the rays refracted in the lower crust was calculated (Figure 13). It is worth noting here that this test gives the uncertainty in the average depth of the boundary, not in the depth variations along the boundary. However, because the calculated rays fit well the slopes of the observed refracted phases in the lower crust (Figures 10 and 11), the shape of the top of the lower crustal layer or, equivalently, the depth variations along this boundary cannot be resolved better than they are. The uncertainty in the top of the lower crustal layer varies depending on the area (Figures 13a and 13b) and is less than ±1 km.

[34] We also calculated the uncertainty in the depth of the Moho, assuming a picking uncertainty of 120 ms. For this we calculated the T_{RMS} residual, moving the entire Moho interface up and down. The uncertainty in the depth of the Moho is less than ±0.5 km (Figure 13c). The T_{RMS} misfit between all observed and calculated travel times is 73 ms, and the χ^2 value associated with our estimated travel time uncertainties is 1.262.

5. Discussion

[35] In sections 5.1–5.3 we discuss the nature of the crust in the center of the GIB and the origin of the two different crustal structures at both flanks of the basin. Subsequently, we use this information, together with the MCS depth

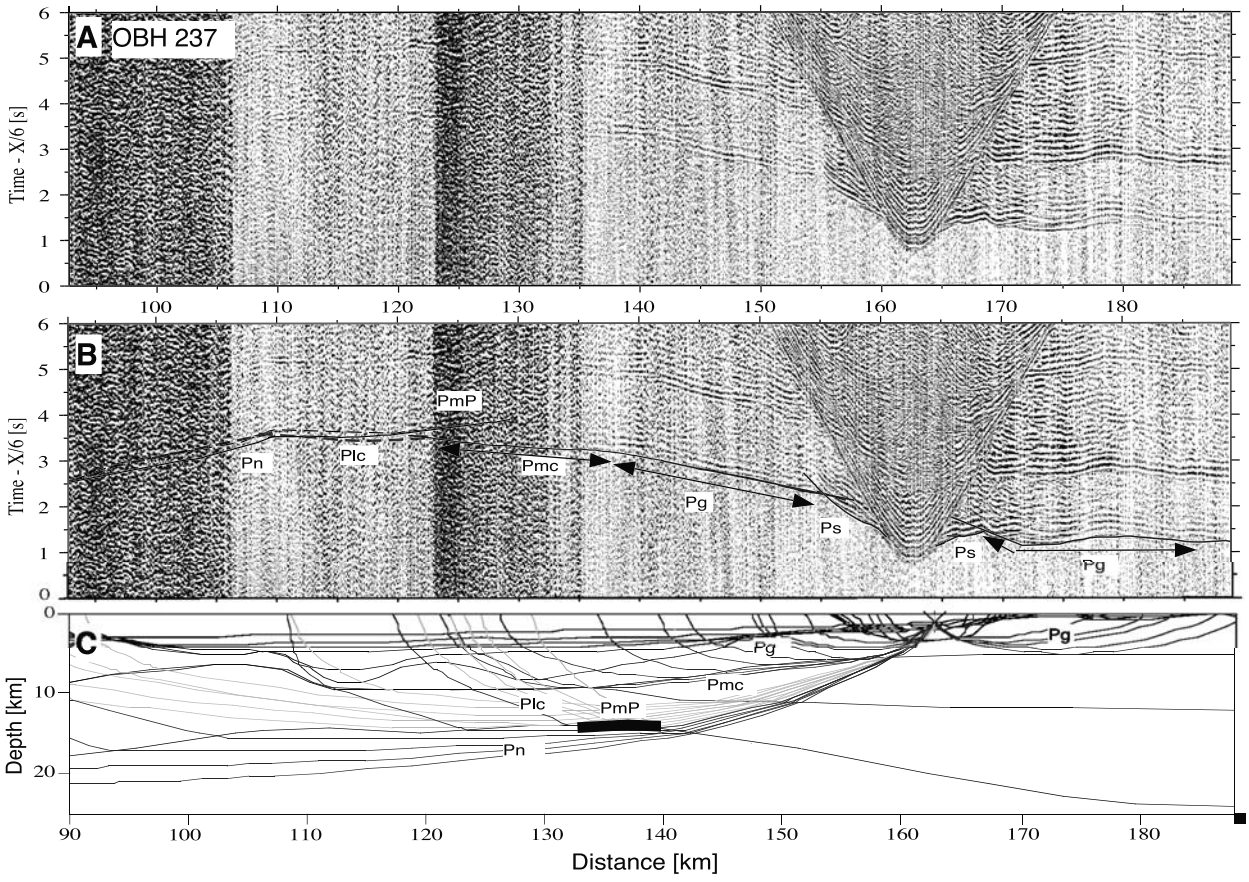

Figure 7. Same as in Figure 5 but for OBH 237. *Ps* are refracted arrivals in the sediments.

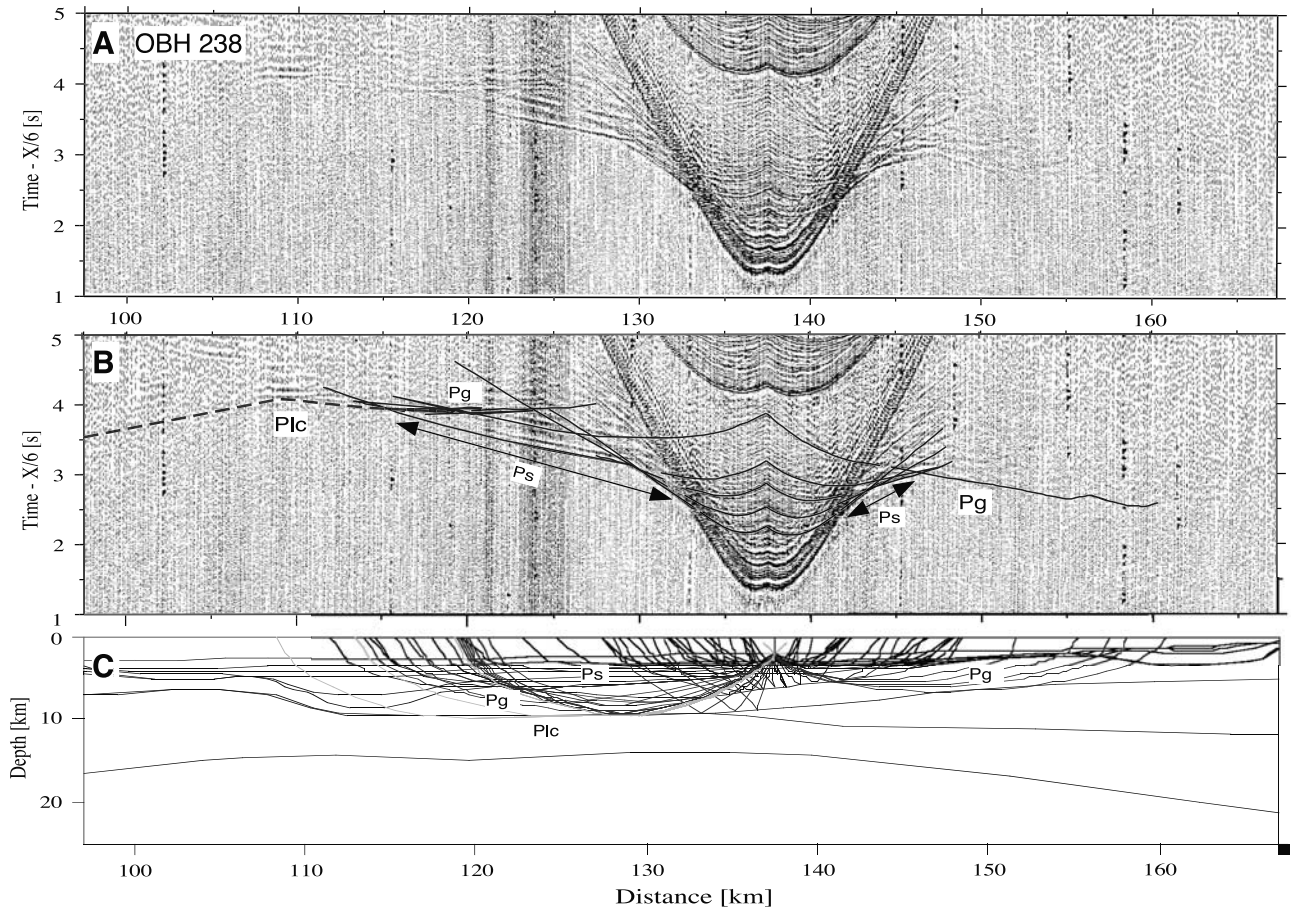

Figure 8. Same as in Figure 5 but for OBH 238.

images and the velocity structure, to discuss the mechanisms of extension in the basin.

5.1. Nature of the Crystalline Crust

[36] At the center of the basin, eastward of fault F3, the crust thins to 6–8 km on blocks B1–B2 ($\beta \sim 4$ to ~ 5.5, Figure 4c), relative to the 32-km-thick onshore crust [*Córdoba et al.*, 1988]. Similar blocks have been observed at the continent-ocean transition (COT) of the West Iberia margin [*Krawczyk et al.*, 1996; *Chian et al.*, 1999]. Here drilling results combined with wide-angle data confirmed that they consist of continental crust underlain by serpentinized mantle [*Chian et al.*, 1999], giving way laterally to unroofed mantle [*Whitmarsh and Wallace*, 2001]. Hence part of the basement of blocks B1 and B2 might consist of serpentinized mantle implying stretching factors larger than ~4–5.5. Since serpentinites can have a wide range of velocities depending on the degree of serpentinization (4.5 to <8 km/s), the absolute velocities are not sufficient to distinguish between continental crust and serpentinized mantle.

[37] One way to distinguish between different crustal types is by comparing their velocity gradients. Drilling results and wide-angle data in the COT of the Iberia Abyssal Plain indicate that the basement mainly consists of serpentinized mantle [*Dean et al.*, 2000; *Chian et al.*, 1999; *ODP Leg 173 Scientific Party*, 1998]. There the basement has a velocity structure with two layers, with gradients and velocity distribution that differ from both continental and oceanic crust (Figure 14a). The velocity structure at the center of the GIB (zone II, Figures 4 and 14a) is different from that at the COT of Iberia Abyssal Plain. The upper layer has a maximum thickness of 3 km and a velocity ranging from 5.3 to 6.3 km/s, with a low-velocity gradient in comparison to serpentinized basement (Figure 14a). The lower crustal layer is ~5 km thick and has velocities from 6.6 to 6.9 km/s and a low-velocity gradient typical of lower continental crust [*Christensen and Mooney*, 1995]. Moreover, no gradual increase toward velocities of 8 km/s is observed, and Moho reflections form this area are seen at OBH 240 (Figure 10) and OBH 237 (Figure 7). In contrast, the velocity structure at the center of the basin is similar to that in other areas of extended continental crust (Figure 14b), suggesting that the entire thin crust at the center of the basin is continental.

5.2. Formation of the GIB

[38] The morphology and structure of GIB is markedly asymmetric: much of the large-scale faulting occurred west of km 130 (zone II, Figure 4), whereas top basement at the east flank of the basin is little faulted and deepens smoothly toward the basin center. Also, the layers with velocities ranging from ~5.0 to 6.2–6.3 km/s are thicker at zone I than at the zone III (Figure 4a).

[39] The velocity structure beneath the continental shelf (zone I, Figures 4 and 14c) is similar to that of the onshore Variscan Central Iberian zone [*Córdoba et al.*, 1988]. The

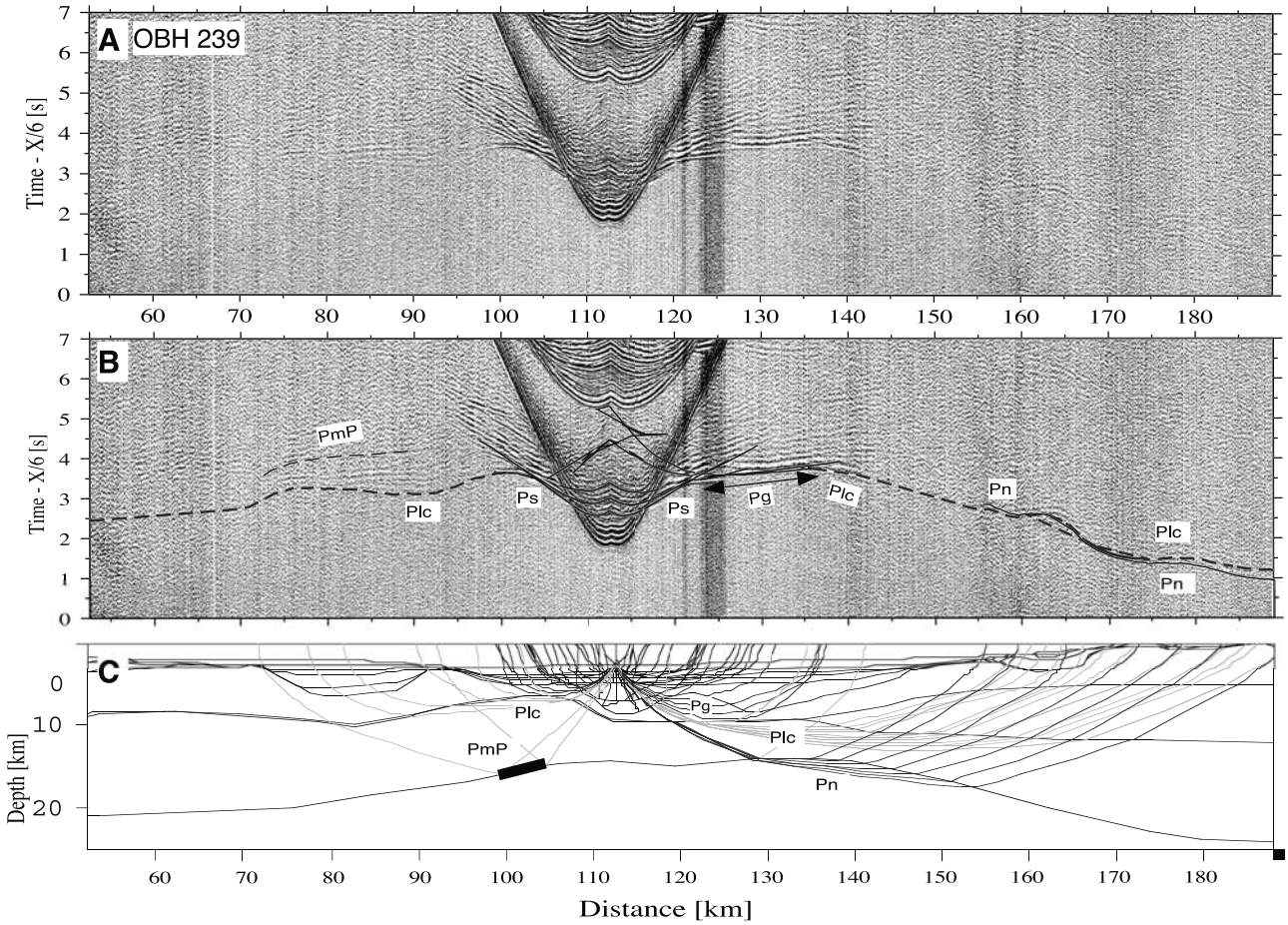

Figure 9. Same as in Figure 5 but for OBH 239.

velocity structure at the east and west flanks of Galicia Bank is similar (Figure 14c). Since the crust at both flanks of the GIB is little extended (stretching factor <2, Figure 4b), the differences in velocity structure may reflect the different nature of the crust in zone I, the shelf area, and zones II and III, deep basin and east flank of Galicia Bank.

[40] The distribution of Variscan terrains on shore suggests that the continental shelf is within the Central Iberian terrain, whereas samples from Galicia Bank indicate that the basement there is the northward continuation of the Ossa Morena terrain [*Capdevila and Mougenot*, 1988] (Figure 1). We suggest that extension of the GIB focused along a suture separating the Central Iberian terrain from the Ossa Morena terrain and that the change in velocity structure reflects the change in crustal type of the two different terrains.

5.3. Mechanisms of Extension of the GIB

[41] As mentioned in section 1, several models have been proposed to explain how the crust deforms with increasing extension at nonvolcanic margins, which formed, where the crust was rather thin and cold prior to rifting. We use the combined tectonic and velocity structure, in addition to results from numerical modeling, to infer the mechanisms of thinning at the GIB. In doing so, we assume that we can correlate the upper, middle, and lower wide-angle seismic velocity layers with the upper, middle, and lower petrological crustal layers (UC, MC, and LC, respectively, Figure 4c). This assumption relies on laboratory measurements of velocities in different rock types. The 6.0–6.3 km/s velocities observed in the upper and middle velocity layers along line 17 (Figure 4a) are commonly observed on seismic profiles at upper and middle crustal depths and are also measured in laboratory experiments in granites and granodiorites which occur in the upper and middle crust [*Christensen and Mooney*, 1995; *Hurich et al.*, 2001]. Fracturing and related alteration is most probably responsible for the lowering in velocities to 5–5.3 km/s at top basement along line 17. The velocities of ~6.6–6.9 km/s at the lower wide-angle layer along line 17 are measured in rocks of more mafic composition such as anorthosites, thought to compose the lower continental crust [*Christensen and Mooney*, 1995]. Thus we use seismic velocities to infer crustal petrology. By doing so, we assume that varying degrees of hydration and fracturing have not significantly affected velocities in the middle-lower crust and also that large modification of the velocities by magmatic intrusions is probably negligible since there is little evidence for synrift magmatism at the margin [*Whitmarsh and Wallace*, 2001].

5.3.1. Evolution of Crustal Rheology From Combined MCS and Wide-Angle Interpretation

[42] To understand the deformation of the crustal layers from the little extended rift flanks ($\beta \sim 1.5–2$) to the highly stretched basin center ($\beta \sim 4–5.5$), we overlaid the interpretation of the MCS depth section on the wide-angle

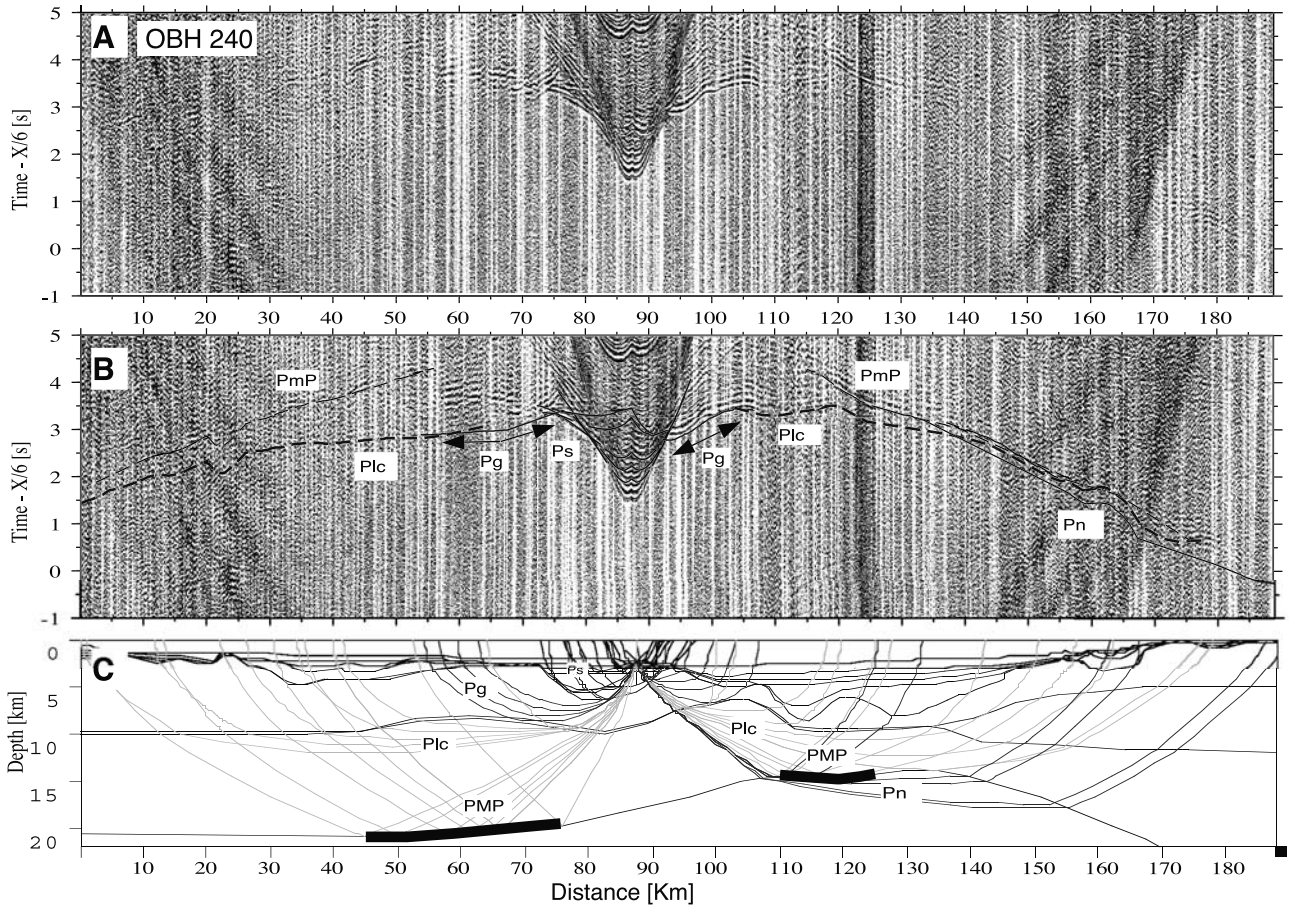

Figure 10. Same as in Figure 5 but for OBH 240.

velocity model (Figure 4). Under the little extended rift flanks ($\beta \sim 1.5-2$), faults imaged in the prestack depth-migrated section occur within the UC but do not appear to reach into the LC, supporting the commonly accepted idea that the UC deforms brittlely and the LC deforms ductily (Figure 4c). Toward the center of the basin, as extension increased, a set of gently dipping, continuous reflections occurs within the LC (DR in Figures 2 and 4c). Fault F5 seems to mark the eastern limit of this reflectivity pattern which does not coincide with a clear wide-angle velocity limit and is not observed under the eastern flank of Galicia Bank (Figures 2 and 3). The origin of lower crustal reflectivity has been debated for some time [e.g., *Blundell*, 1990]. Although it is generally accepted that the ultimate causes of the reflections are lithological contrasts in the lower crust, the process responsible for ordering those contrasts into a reflective fabric may be either intrusive processes [e.g., *Warner*, 1990] or deformation [*Reston*, 1990, 1988]. Given the lack of igneous activity during rifting, we interpret the lower crustal reflectivity in the GIB to represent a ductile deformation fabric formed by shearing of the lower crust.

[43] Toward the center of the basin, block size decreases as the crust thins to 6 km. Faults F1–F4 cut to progressively deeper levels and appear to bring high-velocity LC rocks to shallow depths within their footwall (Figure 4c). This indicates progressive embrittlement of the LC with increasing extension. Rocks that initially deformed ductily were progressively brought to shallower levels and thus cooled and decompressed and the stress difference required to deform brittlely became less than that to deform ductily [*Pérez-Gussinyé and Reston*, 2001]. The DR fabric is not observed beneath the center of the basin (km ~110–130, Figure 2), indicating that either the ductile fabric never existed at this location or that it was intensively fractured by later deep penetrating faults F1–F4 (Figures 2 and 3).

5.3.2. Evolution of the LC Rheology From Numerical Modeling

[44] The evolution of the LC during extension depends on the crustal thickness, the temperature profile at the start of rifting, and the rate of extension [*Pérez-Gussinyé et al.*, 2001]. We suggest that the West Iberia margin was a cold margin because it developed within the ancient Variscan front [*Lefort*, 1984], ~150 m.y. after orogenesis, enough time for the lithosphere to have thermally reequilibrated. Currently, the crustal thickness onshore west Iberia is 32 km [*Córdoba et al.*, 1988]. Estimates of erosion since the Variscan, based on the depth of intrusion of late orogenic plutonic rocks currently exposed at the surface, are on the order of 6 km [*Vigneresse*, 1999]. Taking into account that erosion must have been much faster just after the orogeny, the crustal thickness at the beginning of rifting must have been at most 34–35 km. Assuming that no thermal anomalies affected the crust during rifting, extension must have proceeded in a crust that was relatively thin and cold (500–600°C at the crust-mantle boundary). The lack of

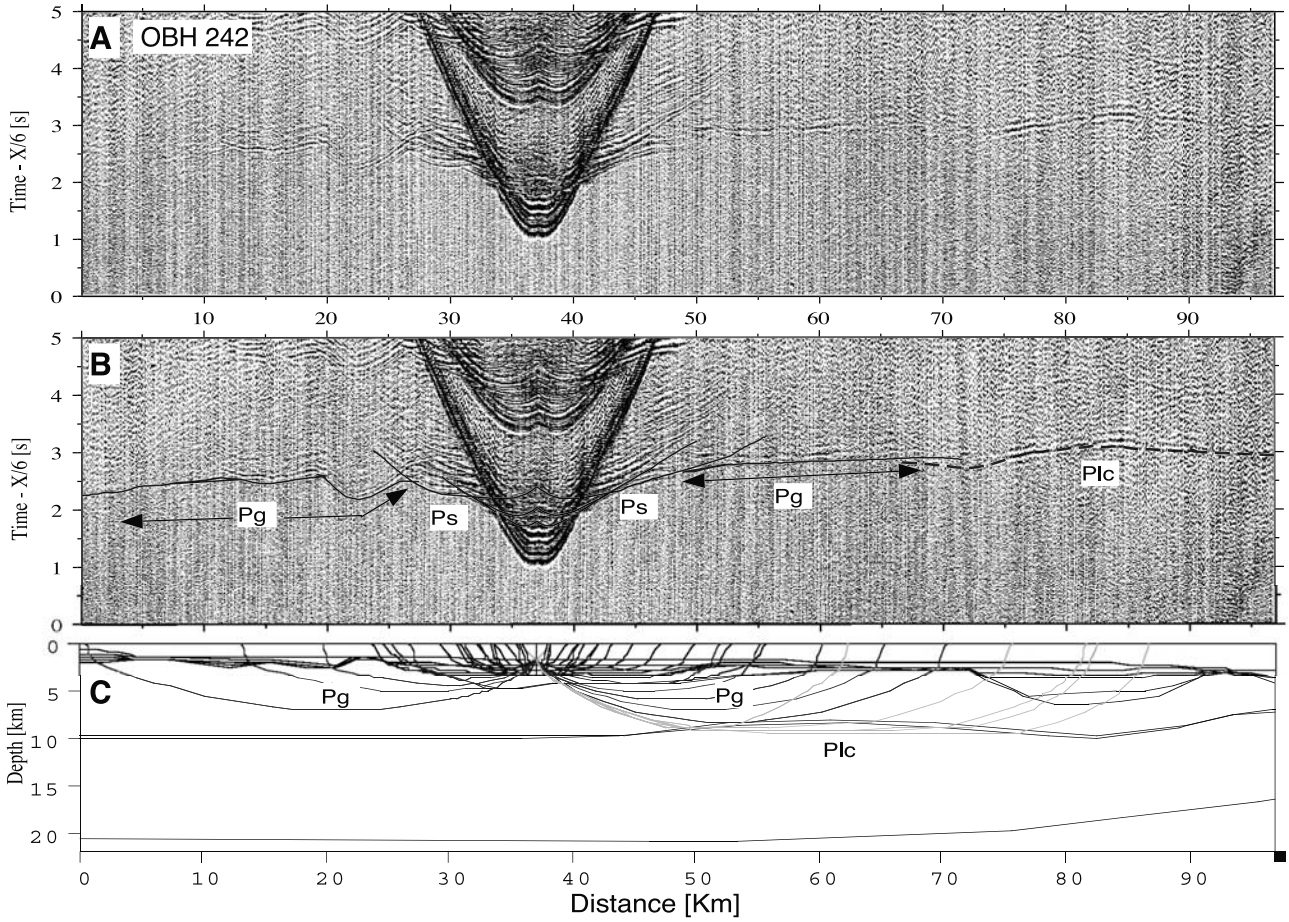

Figure 11. Same as in Figure 5 but for OBH 242.

evidence of synrift magmatism and the presence of serpentinites at the base of the crust during the last stages of rifting at the margin [*Boillot et al.*, 1989; *Chian et al.*, 1999] support the idea that the lithosphere was cold and the crust thin at the start of rifting [*Pérez-Gussinyé et al.*, 2001].

[45] Numerical modeling of the rheological evolution of the crust during extension for an initial crustal thickness of

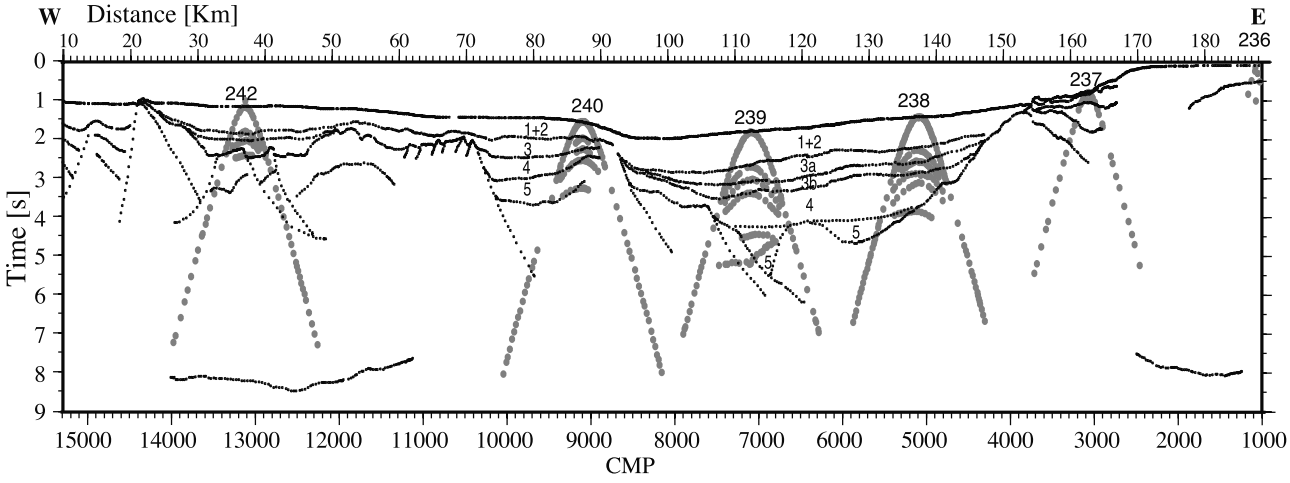

Figure 12. Correspondence between sedimentary formations and top basement interpreted in the MCS data (black dots) and near-offset reflections (gray dots) interpreted on OBH record sections. The wide-angle reflections from the sedimentary layers and top basement were identified along the coincident MCS time section. The corresponding MCS reflectors were digitized and converted to OBH geometry [*Kopp*, 1997].

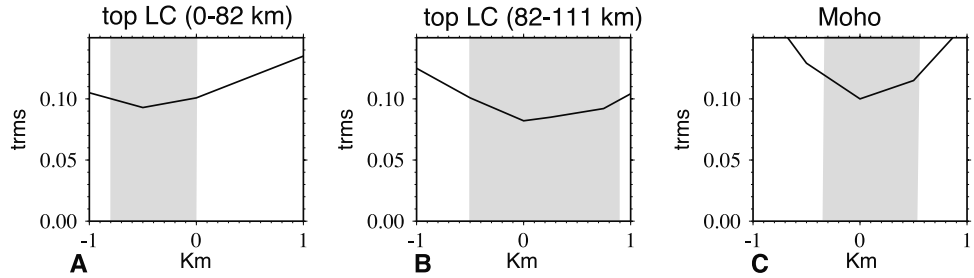

Figure 13. Uncertainty in (a) depth top lower crust (LC) between km 0 and 82 of the model, (b) depth to top lower crust between km 82 and 111, and (c) the Moho depth. Depth uncertainties are those depths for which the T_{RMS} misfit is <100 ms for the lower crust and 120 ms for the Moho (gray shaded areas). These uncertainties correspond to one period of the lower crust refracted arrivals and the reflected arrivals in the Moho, respectively.

32 km, a temperature at the crust-mantle boundary of 515°C and a range of rift durations inferred for the GIB (5–19 m.y. [*Murillas et al.*, 1990]) predicts that the entire crust enters the brittle regime of deformation at stretching factors of ~3.5 to ~5 assuming a lower crust rheology between that of anorthosite and dry quartz (Figure 15a). Changing the crustal thickness to 35 km or increasing the temperature at the Moho by 50°C does not significantly change this result [*Pérez-Gussinyé and Reston*, 2001]. These stretching factors are comparable to those measured at the center of the GIB (km 110 to 130, Figure 2), where faults appear to cut deep in the crust. Thus the modeling supports the interpretation that a large part of the LC rocks switched to brittle deformation mechanisms as they cooled and decompressed during extension.

[46] Several conceptual models of the evolution of deformation at nonvolcanic margins suggest that a large part of the lower crust is squeezed out of the center of the basin toward the basin flanks at the start of rifting [*Manatschal and Bernoulli*, 1999; *Whitmarsh et al.*, 2000] or during the entire rifting period [*Brun and Beslier*, 1996], creating a large deficit of LC at the center of the basin. This process would imply outward flow of the LC over large distances (~100 km). However, our data show that at the GIB, there

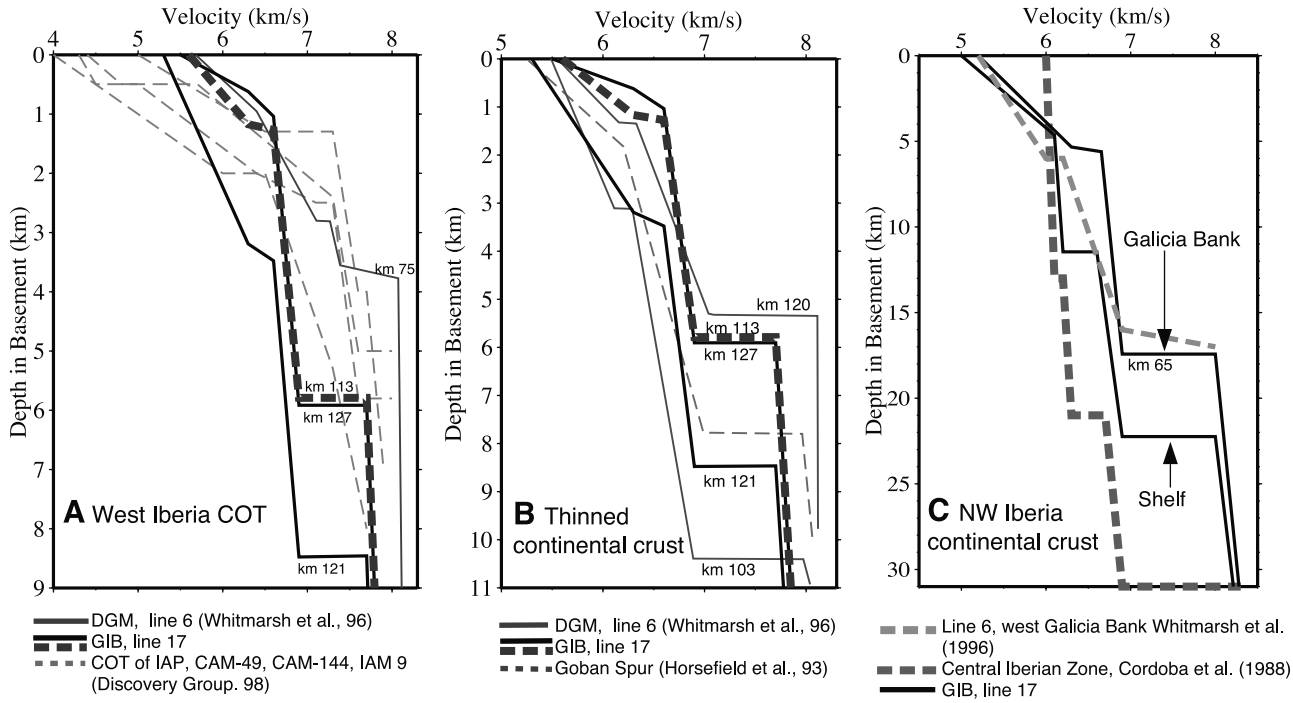

Figure 14. (a). One-dimensional velocity profiles at highly stretched crust along line 17 (zone II, km indicate position along line 17) and at the continent-ocean transition (COT) of the Iberia Abyssal Plain and the Deep Galicia Margin. (b) The same as in Figure 14a but for line 17 and velocity profiles at stretched continental crust at the slope Goban Spur and at the western slope of Galicia Bank. (c) One-dimensional depth velocity profiles at flanks of the Galicia Interior Basin (GIB) (km indicate position along line 17), at the continental crust onshore (Central Iberia zone), and at the west flank of Galicia Bank.

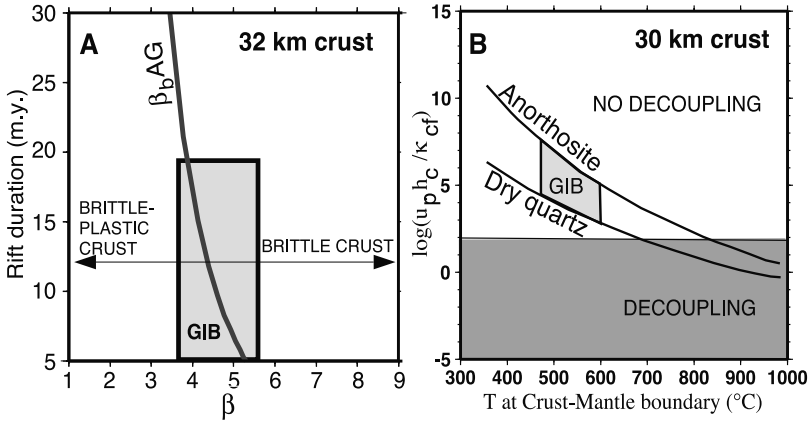

Figure 15. (a) The line β_bAG indicates stretching factors at which the entire crust becomes brittle for different rift durations, an aggregate rheology (50% dry quartz, 50% anorthosite) for the lower crust and a temperature structure adequate for West Iberia (section 5.3.2 and *Pérez-Gussinyé and Reston* [2001]). The gray box comprises the possible range of stretching factors and rift durations at the center of the GIB (zone II, Figure 2). (b) Initial temperature conditions at the crust-mantle boundary for large-scale lower crustal flow assuming a 30-km crust and a lower crustal rheology consisting of anorthosite or dry quartz. Decoupling only occurs when the ratio of advective thinning rate, ($u_p h_0$), to diffusion constant for lower crustal flow, κ_{cf}, is <100. When this ratio is big, lower crustal flow cannot keep up with crustal thinning and large-scale flow does not occur (u_p, plate spreading velocity; h_0, crustal thickness; see *Hopper and Buck* [1998] for a detailed explanation). Decoupling only occurs when the prerift temperature at the crust-mantle boundary is higher than 700°C (dry quartz) or 900°C (anorthosite), much higher than the 500–600°C estimated for the west Iberia margin at the start of rifting (section 5.3.2 and *Pérez-Gussinyé et al.* [2001]). This suggests that at the GIB large-scale crustal flow was unlikely; instead most of the crust might have entered the brittle regime at the center of the basin.

is no overall deficit of LC at the center of the basin (km 90–140, Figure 4c). Instead, as extension factors increase, there are local excesses of LC that coincide with basement lows (km ~95–118 and ~126–135, Figure 4c and section 5.3.3). Hence, if LC flow occurred, it must have been directed toward the center of the basin. Lower crustal flow over ≥100 km toward the center of a basin has been inferred to occur during postorogenic extension of thick crust that produced the Basin and Range [*Gans*, 1987]. Numerical modeling results show that large-scale LC flow (for ≥100 km) only occurs when the crust is thick and warm or when the LC rheology is extremely weak [*Kusznir and Matthews*, 1988; *Kruse et al.*, 1991; *Hopper and Buck*, 1998; *McKenzie et al.*, 2000]. *Hopper and Buck* [1998] estimate that for large-scale LC flow to occur, the lower limit temperature at the crust-mantle boundary prior to rifting for a 30-km and 50-km-thick crust is 700–800°C and 600–700°C, respectively, for a LC rheology between dry quartz and anorthosite. These estimates are similar to those obtained by *Kruse et al.* [1991], *Kusznir and Matthews* [1988], and *McKenzie et al.* [2000] and are much higher than those inferred for the GIB (Figure 15b), thus supporting the hypothesis that large-scale lower crustal flow toward the center of the basin could not have occurred here and probably along the entire margin.

5.3.3. Differential Versus Nondifferential Stretching of UC and LC

[47] To assess the importance of differential crustal extension we have investigated how the ratio of upper to lower crust varies across the basin (UC/LC, Figure 4b). The accuracy of this ratio is dependent on the resolution with which the UC-LC boundary is determined. It is also dependent on the accuracy of the Moho and of the basement relief, but these, especially the latter, are better resolved. For instance, in the extreme case where the basement relief were fully resolved but the upper crust/lower crust interface were very poorly resolved, the UC/LC ratio might reflect the basement relief but not the relative variations in thickness of the these layers. However, where the ray coverage is good enough, a smoothed version of the upper-lower crust relief can be resolved by the data. Thus we expect that the UC/LC ratio will be better determined in the center of the basin where the ray density is greatest. However, even at km 30–70 and km 160–180, where the ray coverage is poorer, error analysis indicates that possible undulations of the UC-LC interface are less than 1 km, allowing us to place error bars on the UC/LC ratio. Despite the limitations of this method, we believe that estimates of the amount of stretching derived in this manner are likely to be more reliable than any that rely on inferring the amount of extension from the geometry of the few faults that are well imaged.

[48] The UC-LC interface shows little relief at the little extended regions (km 30–70 and 160–180, Figure 4c) either side of the GIB. Even if the UC/LC ratio is less reliable here than in the center of the basin, the structure on the margins of the basin is also simpler, with a smooth top basement and subhorizontal Moho, implying that the smooth upper-lower crust relief at the rift flanks is not just a result of poor resolution but reflects a lack of abrupt variations ($\beta \sim 1.5$–2, km 30–70 and 160–180, Figure 4b). Thus the low variation in UC/LC ratio along the rift flanks indicates that extension of the UC and LC was uniform in

these areas (km 30–70 and 160–180, Figure 4). Furthermore, the velocity structure between 160 and 180 km can be extended farther to the east by the results of *González et al.* [1999] and remains remarkably constant. (Note that the different ratios east and west of the GIB are a result of assuming UC + MC as upper crust at the Central Iberian terrane and reflect the different velocity structure of the crust either side of the basin (Figure 4).)

[49] As the UC/LC ratio on each basin flank remains constant even as the edge of the basin is approached, we can immediately rule out the possibility of large-scale displacement of the lower crust either toward or away from the basin: the lower crust between km 30–90 and 160–180 has not been thickened or thinned excessively. Thus any local excess of the LC between km 90 and 160 must be matched by a corresponding LC deficit within the same region.

[50] In the region between km 90 and 160 we do observe significant variations in the UC/LC ratio, with a general excess of the lower crust beneath the western and central parts of the basin (km 95–135), and a deficit beneath the eastern side of the basin (km 135–160). As discussed in section 4.3.2, refracted arrivals observed at OBH 240 (km ~105–117, Figure 10) indicate a high-velocity zone at very shallow depths in the basement (6.6–6.9 km/s velocities at blocks B3–B4, Figure 4). Also, refracted arrivals observed on OBH 239 (km ~135–145, Figure 9) and OBH 237 (km ~120–110, Figure 7) require high velocities (~6.6–6.9 km/s) very close to top basement (km ~125–135, Figure 4c). Thus we believe that the top of the lower crust within the footwalls of faults F3–F4 and F1 is well constrained (Figures 4b and 4c). However, we do not believe that this pattern requires significant lateral flow of the lower crust but rather that it reflects the net effect of the observed array of east-dipping faults that cut into and offset the lower crust.

[51] Movement along an isolated east dipping normal fault cutting deep into the lower crust results in the displacement up and to the west of the lower crust in the footwall relative to the upper crust of the hanging wall. Such displacements are necessarily accompanied by local ductile deformation of the lower crust at the base of the fault blocks to maintain a relatively smooth Moho. Were such a fault isolated, we would expect to observe a clear LC excess in the footwall and a LC deficit in the hanging wall. However, within the GIB, the faults do not exist in isolation but rather as an array of east dipping faults, so that any individual fault block might represent the hanging wall to one fault and the footwall to the other. As our data cannot completely resolve the detailed distribution of the lower crust within individual fault blocks, the generation of a net excess or deficit of the lower crust within a fault-bound block depends on the relative importance of the two faults. For instance, we relate the local excess of LC at km 95–110 to the uplift of LC to shallow levels along a major brittle fault system (F3–F4, Figure 4). As the partial exhumation of LC within the footwall of a fault should produce a deficit of LC in the hanging wall, the LC excess in the footwall to F3–F4 might be expected to be matched by a LC deficit in the hanging wall, i.e., in block B2. However, block B2 is also in the footwall to F1, and as we only resolve the net effect resulting from the block-bounding faults, the LC deficit in the hanging wall to F3 is not fully resolved.

[52] The net effect on the amount of lower crust (excess or deficit) is related to the amount of extension along the fault systems: where the stretching factor increases in the direction of the fault dip, we can expect a net LC excess; where the stretching factor starts to drop in the same direction, we can expect a net LC deficit. This is what we observe: Where β increases toward the east, we have a net lower crustal excess; where β starts to drop to the east, we observe a LC deficit. Only east of F1 (in the region between 137 and 157 km), where there are no major faults and where the stretching factor steadily decreases to the east, can we resolve a LC deficit.

[53] An important part of this process is the ductile deformation or small-scale flow of the lower crust at the base of the fault blocks to maintain a smooth Moho topography. This small-scale flow is driven by the brittle deformation of the overlying crust since it moves lower crust toward the west in order to fill the gaps created by the faulting of the overlying crust. Thus it implies a strong coupling between the ductile and brittle parts of the crust. As such it is quite different from the sort of large-scale lower crustal flow proposed by others, in which the lower crust is effectively decoupled from the upper crust and the patterns of brittle extension. Small-sale flow (~<40 km) of the deepest part of the lower crust does not need the high temperatures required by large-scale flow [*McKenzie et al.*, 2000] and has also been inferred to explain footwall and Moho uplift accompanying crustal thinning at the Bay of Biscay margin [*ter Voorde et al.*, 1998].

5.4. Evolution of Extension at the West Iberia Margin

[54] The GIB represents a case example of rifting of a cold and thin crust from $\beta \sim 1.5$ up to ~3.5–5.5 and thus provides a link between little extended areas and areas where final continental breakup occurs. In this section we integrate the results from the GIB and the final breakup segments of the West Iberia margin (where $\beta > 5$) to describe the evolution of the mechanisms of extension from the little extended shelf to the final breakup margins.

[55] At the start of rifting, upper crustal rocks deformed brittlely, and lower crustal rocks deformed ductily. However, large-scale lower crustal flow ($\geq$100 km) did not occur, as evidenced by a lack of either an overall excess or deficit of lower crust over most of the section. The temperature at the crust-mantle boundary at the GIB was probably much lower than that required for this kind of flow to occur. The UC/LC ratio was maintained at low stretching factors ($\beta < 2$) so that extension occurred by large-scale uniform pure shear. As extension increased, lower crustal rocks cooled, decompressed, and eventually switched to brittle deformation mechanisms [*O'Reilly et al.*, 1996; *Pérez-Gussinyé and Reston*, 2001]. At high stretching factors, $\beta \sim 3.5$, faults reached deep into the crust, bringing LC rocks at shallow levels within the footwall. Simultaneously, small-scale flow (<40 km) of the deepest levels of the lower crust occurred to accommodate the offsets created by the overlying deep penetrating brittle faults. This resulted in an accumulation of LC in the direction opposite to fault dip. At this stage, the upper and lower crust extended by similar amounts at large scale, but simple shear occurred at fault block scale along high-angle, planar (>30°) crustal-scale faults as most of the crust was brittle.

[56] Neither large-scale decoupling of upper and lower crust nor large-scale differential stretching of upper and lower crustal rocks is required by the observations. There is not a large deficit of LC toward the center of the basin nor an accumulation of LC below rift flanks as proposed by *Manatschal and Bernoulli* [1999] and *Whitmarsh et al.* [2000, 2001]. Models suggesting that the UC and LC are decoupled by a detachment level at the brittle-ductile transition during the last stages of rifting [e.g., *Driscoll and Karner*, 1998] are not supported by our observations. Instead, UC and LC rocks become tightly coupled as the LC progressively enters the brittle deformation regime.

[57] With ongoing extension ($\beta > 5$, Deep Galicia Margin and Iberia Abyssal Plain segments, Figure 1) the entire crust became brittle, and LC rocks were exhumed at top basement at the locus of continental break up (e.g., lower crustal rocks drilled at Sites 1067, 1068, and 900 [*Whitmarsh and Wallace*, 2001]). Faults cut into the mantle, allowing large amounts of seawater to serpentinize it [*Pérez-Gussinyé and Reston*, 2001]. The low coefficient of friction of serpentinites and high pore pressures could enable the formation of a low-angle decollement at the crust-mantle boundary [e.g., *Reston et al.*, 1996; *Krawczyk et al.*, 1996]. Rotated blocks made of upper and lower crustal rocks formed by simple shear along high-angle crustal-scale faults detach onto these decollements. These decollements could decouple the deformation in the crust from that in the mantle creating a departure from large-scale pure shear to large-scale nonuniform pure shear in which crust and mantle deform by different amounts [*Pérez-Gussinyé and Reston*, 2001].

6. Conclusions

[58] We have analyzed multichannel seismic reflection and wide-angle data across an abandoned rift, the Galicia Interior Basin, located at the nonvolcanic margin off West Iberia. The data reveal the tectonic and velocity structure of the basin and provide an excellent opportunity to study the mechanisms of thinning from the slightly extended flanks, ($\beta \sim 1.5-2$) to the center of the basin ($\beta \sim 3.5-5.5$). The GIB might be a case example for rifting at nonvolcanic margins that initiated in thin ($\sim$30 km) and cool crust ($\sim$500–600°C at the Moho).

[59] The data show that the structure of the basin is asymmetric. The center of the basin consists of rotated blocks bounded by large eastward dipping faults, whereas top basement east of the basin deepens gradually toward the basin center. The thinnest crust is 6–8 km thick and appears to be continental in nature.

[60] The velocity structure underneath both flanks of the basin is different. Below the continental shelf and slope the upper crustal region with velocities up to 6.2 km/s extends much deeper than at the west flank of the basin. We interpret that these two different crustal types are a result of the inception of the basin along an ancient Variscan suture that separated two different terrains.

[61] We consider that extension occurred as follows:

[62] At small stretching factors ($\beta \leq 1.5-2$), extension occurred by large-scale uniform pure shear accommodated by brittle and ductile deformation in the upper and lower crust, respectively. The ratio of upper to lower crustal rocks is constant during this phase.

[63] With increasing extension, lower crustal rocks entered progressively into the brittle regime. At stretching factors of $\beta \sim 3.5-5.5$, simple shear occurred along deeply penetrating faults as most of the crust became brittle. Lower crustal rocks were brought to shallow levels in the basement creating an excess of lower crust within their footwalls.

[64] Exhumation of lower crust along brittle faults drove small-scale flow (<40 km) of the remaining deep, ductile lower crust in order to accommodate fault offsets. This flow was directed opposite to fault dip direction and resulted in a smooth Moho topography.

[65] The asymmetry in the distribution of lower crust at the basin is self-contained, occurs at a small-scale (<40 km), and is a direct consequence of the exhumation of LC along high-angle brittle faults and the accompanying small-scale flow of the deepest part of the LC.

[66] **Acknowledgments.** We thank John Hopper and Benjamin Holtzman for their comments and suggestions on earlier versions this manuscript. We also thank Tim Minshull and an anonymous reviewer for their comments, which greatly improved the paper. M.P.G. was supported by a EU Marie Curie Fellowship at GEOMAR. The R/V *M. Ewing* cruise was funded by the NSF. The deployment of the Ocean Bottom Hydrophones by financed by the German Research Council (DFG) under grant Re 873/6-1.

References

Artyushkov, E. V., Stresses in the lithosphere caused by crustal thickness in homogeneities, *J. Geophys. Res.*, *78*, 7675–7708, 1973.

Bassi, G., Relative importance of strain rate and rheology for the mode of continental extension, *Geophys. J. Int.*, *122*, 195–210, 1995.

Block, L., and L. H. Royden, Core complex geometries and regional scale flow in the lower crust, *Tectonics*, *9*, 557–567, 1990.

Blundell, D. J., Seismic images of the continental lithosphere, *J. Geol. Soc. London*, *147*, 895–913, 1990.

Boillot, G., and E. Winterer, Drilling on the Galicia margin: Retrospect and prospect, *Proc. Ocean Drill. Program Sci. Results*, *103*, 809–828, 1988.

Boillot, G., G. Feraud, M. Recq, and J. Girardeau, "Undercrusting" by serpentinite beneath rifted margins: The examples of the west Galicia margin (Spain), *Nature*, *431*, 523–525, 1989.

Braunmiller, J., and J. Nábìlek, Geometry of continental normal faults, *J. Geophys. Res.*, *101*, 3045–3052, 1996.

Brun, J. P., and M. O. Beslier, Mantle exhumation at passive margins, *Earth Planet. Sci. Lett.*, *142*, 161–173, 1996.

Buck, W. R., Modes of continental extension, *J. Geophys. Res.*, *96*, 20,161–20,178, 1991.

Capdevila, R., and D. Mougenot, Pre-Mesozoic basement of the western Iberian continental margin and its place in the Variscan belt, *Proc. Ocean Drill. Program Sci. Results*, *103*, 3–12, 1988.

Chian, C., K. E. Louden, T. A. Minshull, and R. B. Whitmarsh, Deep structure of the ocean-continent transition in the southern Iberia Abyssal Plain from seismic refraction profiles: Ocean Drilling Program (Legs 149 and 173) transect, *J. Geophys. Res.*, *104*, 7443–7462, 1999.

Christensen, N., and W. Mooney, Seismic velocity structure and composition of the continental crust: A global view, *J. Geophys. Res.*, *100*, 9761–9788, 1995.

Córdoba, D., E. Banda, and J. Ansorge, *P*-wave velocity-depth distribution in the Hercynian crust of northwest Spain, *Phys. Earth Planet. Inter.*, *51*, 235–248, 1988.

Dean, S. M., T. A. Minshull, R. B. Whitmarsh, and K. E. Louden, Deep structure of the ocean-continent transition in the southern Iberia Abyssal Plain from seismic refraction profiles: The IAM-9 transect at 40°20′N, *J. Geophys. Res.*, *105*, 5859–5885, 2000.

Denelle, E., Y. Dezard, and J. Raoult, 2-D prestack depth migration in the (S-G-W) domain, paper presented at the 56th Meeting, Soc. of Explor. Geophys., Houston, Tex., 1986.

Discovery 215 Working Group, Deep structure in the vicinity of the ocean-continent transition in the southern Iberia Abyssal Plain, *Geology*, *26*, 743–746, 1998.

Driscoll, N. W., and G. D. Karner, Lower crustal extension across the northern Carnarvon basin, Australia: Evidence for an eastward dipping detachment, *J. Geophys. Res.*, *103*, 4975–4991, 1998.

England, P., Constraints on extension of continental lithosphere, *J. Geophys. Res.*, *88*, 1145–1152, 1983.

Flueh, E. R., and J. Bialas, A digital, high data capacity ocean bottom recorder for seismic investigations, *Int. Underwater Syst. Design*, *18*(3), 18–20, 1996.

Gans, P. B., An open-system, two-layer crustal stretching model for the eastern Great Basin, *Tectonics*, *6*, 1–12, 1987.

González, A., D. Cordoba, and D. Vales, Seismic crustal structure of Galicia continental margin, NW Iberian Peninsula, *Geophys. Res. Lett.*, *26*, 1061–1064, 1999.

Gradstein, F. M., F. P. Agterberg, J. G. Ogg, J. Hardenbol, P. van Veen, J. Thierry, and Z. Huang, A Mesozoic time scale, *J. Geophys. Res.*, *99*, 24,051–24,074, 1994.

Hopper, J. R., and W. R. Buck, The effect of lower crustal flow on continental extension and passive margin formation, *J. Geophys. Res.*, *101*, 20,175–20,194, 1996.

Hopper, J. R., and W. R. Buck, Styles of extensional decoupling, *Geology*, *26*, 699–720, 1998.

Horsfield, S. J., R. B. Whitmarsh, R. S. White, and J. C. Sibuet, Crustal structure of the Goban Spur rifted continental margin, NE Atlantic, *Geophys. J. Int.*, *119*, 1–19, 1993.

Hubral, P., Time migration: Some ray theoretical aspects, *Geophys. Prospect.*, *25*, 738–745, 1977.

Hurich, C. A., S. J. Deemer, and A. Indares, Compositional and metamorphic controls on velocity and reflectivity in the continental crust: An example from the Greenville Province of eastern Québec, *J. Geophys. Res.*, *106*, 665–682, 2001.

Jackson, J. A., Active normal faulting and crustal extension, in *Continental Extensional Tectonics*, edited by M. P. Coward, J. F. Dewey, and P. L. Hancock, *Geol. Soc. Spec. Publ.*, *28*, 3–17, 1987.

Kopp, C., Struktur und tektonische Mechanismen der Nord-Sulawesi Subduktionszone (Indonesien), Ph.D. thesis, Univ. of Kiel, Kiel, Germany, 1997.

Krawczyk, C. M., T. J. Reston, M. O. Beslier, and G. Boillot, Evidence for detachment tectonics on the Iberia Abyssal Plain rifted margin, *Proc. Ocean Drill. Program Sci. Results*, *149*, 603–615, 1996.

Kruse, S., M. McNutt, J. Phipps Morgan, L. Royden, and B. Wernicke, Lithospheric extension near Lake Mead, Nevada: A model for ductile flow in the lower crust, *J. Geophys. Res.*, *96*, 4435–4456, 1991.

Kusznir, N. J., and D. H. Matthews, Deep seismic reflections and the deformational mechanics of the continental lithosphere, *J. Petrol., Special Lithosphere Issue*, 63–87, 1988.

Kusznir, N. J., A. M. Roberts, and C. K. Morley, Forward and reverse modeling of rift basin formation, in *Hydrocarbon Habitat in Rift Basins*, edited by J. J. Lambiase, *Geol. Soc. Spec. Publ.*, *80*, 33–56, 1995.

Lefort, J. P., The main basement features recognized in the northern part of the North Atlantic area, *Initial Rep. Deep Sea Drill. Proj.*, *80*, 1103–1114, 1984.

Luetgert, J. H., MacRay—Interactive two-dimensional seismic raytracing for the Macintosh, *U. S. Geol. Surv. Open File Rep.*, *92-356*, 1992.

Manatschal, G., and D. Bernoulli, Architecture and tectonic evolution of nonvolcanic margins: Present-day Galicia and ancient Adria, *Tectonics*, *6*, 1099–1119, 1999.

McKenzie, D., F. Nimmo, J. Jackson, P. B. Gans, and E. L. Miller, Characteristics and consequences of flow in the lower crust, *J. Geophys. Res.*, *105*, 11,029–11,046, 2000.

Murillas, J., D. Mougenot, G. Boillot, M. C. Comas, E. Banda, and A. Mauffret, Structure and evolution of the Galicia Interior Basin (Atlantic western Iberian continental margin), *Tectonophysics*, *184*, 297–319, 1990.

ODP Leg 173 Shipboard Scientific Party, Drilling reveals transition from continental breakup to early magmatic crust, *Eos Trans, AGU*, *79*(173), 180–181, 1998.

O'Reilly, B. M., F. Hauser, A. W. B. Jacob, and P. M. Shannon, The lithosphere below the Rockall Trough: Wide-angle seismic evidence for extensive serpentinisation, *Tectonophysics*, *255*, 1–23, 1996.

Pérez-Gussinyé, M., Continental rifting and break-up at the West Iberia margin: An integrated geophysical study, Ph.D. thesis, Univ. of Kiel, Kiel, Germany, 2000.

Pérez-Gussinyé, M., and T. J. Reston, Rheological evolution during extension at passive non-volcanic margins: Onset of serpentinization and development of detachments to continental breakup, *J. Geophys. Res.*, *106*, 3961–3975, 2001.

Pérez-Gussinyé, M., T. J. Reston, and J. P. Morgan, Serpentinisation and magmatism at non-volcanic margins—The effect of the initial lithospheric structure, in *Non-volcanic Rifting of Continental Margins: A Comparison of Evidence From Land and Sea*, edited by R. C. L. Wilson et al., *Geol. Soc. Spec. Publ.*, *187*, 551–576, 2001.

Reston, T. J., Evidence for shear zones in the lower crust offshore Britain, *Tectonics*, *7*, 929–945, 1988.

Reston, T. J., The lower crust and the extension of the continental lithosphere: Kinematic analysis of BIRPS deep seismic data, *Tectonics*, *9*, 1235–1248, 1990.

Reston, T. J., C. M. Krawczyk, and D. Klaeschen, The *S* reflector west of Galicia (Spain): Evidence from prestack depth migration for detachment faulting during continental breakup, *J. Geophys. Res.*, *101*, 8075–8091, 1996.

Reston, T. J., J. Pennel, A. Stubenrauch, I. Walker, and M. Pérez-Gussinyé, Detachment faulting, mantle serpentinization, and serpentinite-mud volcanism beneath the Porcupine Basin, southwest Ireland, *Geology*, *29*, 587–590, 2001.

Sherwood, J., Depth sections and interval velocities from surface seismic data, *Leading Edge*, *8–9*, 44–49, 1989.

Smith, W. H. F., and D. T. Sandwell, Marine gravity field from declassified Geosat and ERS-1 altimetry (abstract), *Eos Trans. AGU*, *76*(46), Fall Meet. Suppl., F156, 1995.

Sonder, L., and P. G. England, Effects of temperature-dependent rheology on large-scale continental extension, *J. Geophys. Res.*, *94*, 7603–7619, 1989.

ter Voorde, M., R. T. van Balen, G. Bertotti, and S. A. P. L. Cloething, The influence of a stratified rheology on the flexural response of the lithosphere to (un)loading by extensional faulting, *Geophys. J. Int.*, *134*, 721–735, 1998.

Vigneresse, J. L., Intrusion level of granitic massifs along the Hercynian belt: Balancing the eroded crust, *Tectonophysics*, *307*, 277–295, 1999.

Warner, M., Basalts, water or shear zones in the lower continental crust, *Tectonophysics*, *173*, 15–23, 1990.

Whitmarsh, R. B. and P. J. Wallace, The rift-to-drift development of the west Iberia nonvolcanic continental margin: A summary and review of the contribution of Ocean Drilling Program Leg 173, *Proc. Ocean Drill. Program Sci. Results*, *173*, 1–36 [Online], 2001. (Available at http://www-odp.tamu.edu/publications/173_SR/173TOC.HTM).

Whitmarsh, R. B., R. S. White, S. J. Horsefield, J. Sibuet, M. Recq, and V. Louvel, The ocean-continent boundary off the western continental margin of Iberia: Crustal structure west of Galicia Bank, *J. Geophys. Res.*, *101*, 28,291–28,314, 1996.

Whitmarsh, R. B., S. M. Dean, T. A. Minshull, and M. Tompkins, Tectonic implications of exposure of lower continental crust beneath the Iberia Abyssal Plain, northeast Atlantic Ocean: Geophysical evidence, *Tectonics*, *19*, 919–942, 2000.

Whitmarsh, R. B., G. Manatschal, and T. A. Minshull, Evolution of magma-poor continental margins from rifting to seafloor spreading, *Nature*, *413*, 150–154, 2001.

Wilson, R. C. L., R. N. Hiscott, M. G. Willis, and F. M. Gradstein, The Lusitanian Basin of west-central Portugal: Mesozoic and Tertiary tectonic, stratigraphic, and subsidence history, in *Extensional Tectonics and Stratigraphy of the North Atlantic*, edited by A. J. Tankard and H. R. Balkwill, *AAPG Mem.*, *46*, 341–361, 1990.

Zelt, C. A., and R. B. Smith, Traveltime inversion for 2-D crustal velocity structure, *Geophys. J. Int.*, *108*, 16–34, 1992.

M. Pérez-Gussinyé, Department of Earth Sciences, Oxford University, Parks Road, Oxford OX1 3PR, UK. (martap@earth.ox.ac.uk)

C. R. Ranero and T. J. Reston, GEOMAR Research Center for Marine Geosciences, Wischhofstrasse 1-3, D-24148 Kiel, Germany. (cranero@geomar.de; treston@geomar.de)

D. Sawyer, Department of Geology and Geophysics, Rice University, 6100 Main St., Houston, TX 77005-1892, USA. (dale@geophysics.rice.edu)